Chemistry–A European Journal
Full Paper
doi.org/10.1002/chem.202100705

Chemistry Europe
European Chemical Societies Publishing

Applying Unconventional Spectroscopies to the Single-Molecule Magnets, $Co(PPh_3)_2X_2$ (X = Cl, Br, I): Unveiling Magnetic Transitions and Spin-Phonon Coupling

Alexandria N. Bone,[a] Chelsea N. Widener,[a] Duncan H. Moseley,[a] Zhiming Liu,[a] Zhengguang Lu,[b] Yongqiang Cheng,[c] Luke L. Daemen,[c] Mykhaylo Ozerov,[b] Joshua Telser,[d] Komalavalli Thirunavukkuarasu,[e] Dmitry Smirnov,[b] Samuel M. Greer,[b, f] Stephen Hill,[b, g] J. Krzystek,*[b] Karsten Holldack,[h] Azar Aliabadi,[i] Alexander Schnegg,[i, j] Kim R. Dunbar,[k] and Zi-Ling Xue*[a]

Abstract: Large separation of magnetic levels and slow relaxation in metal complexes are desirable properties of single-molecule magnets (SMMs). Spin-phonon coupling (interactions of magnetic levels with phonons) is ubiquitous, leading to magnetic relaxation and loss of memory in SMMs and quantum coherence in qubits. Direct observation of magnetic transitions and spin-phonon coupling in molecules is challenging. We have found that far-IR magnetic spectra (FIRMS) of $Co(PPh_3)_2X_2$ (**Co-X**; X = Cl, Br, I) reveal rarely observed spin-phonon coupling as avoided crossings between magnetic and *u*-symmetry phonon transitions. Inelastic neutron scattering (INS) gives phonon spectra. Calculations using VASP and phonopy programs gave phonon symmetries and movies. Magnetic transitions among zero-field split (ZFS) levels of the $S = 3/2$ electronic ground state were probed by INS, high-frequency and -field EPR (HFEPR), FIRMS, and frequency-domain FT terahertz EPR (FD-FT THz-EPR), giving magnetic excitation spectra and determining ZFS parameters (D, E) and g values. Ligand-field theory (LFT) was used to analyze earlier electronic absorption spectra and give calculated ZFS parameters matching those from the experiments. DFT calculations also gave spin densities in **Co-X**, showing that the larger Co(II) spin density in a molecule, the larger its ZFS magnitude. The current work reveals dynamics of magnetic and phonon excitations in SMMs. Studies of such couplings in the future would help to understand how spin-phonon coupling may lead to magnetic relaxation and develop guidance to control such coupling.

[a] *A. N. Bone, C. N. Widener, D. H. Moseley, Z. Liu, Prof. Z.-L. Xue*
Department of Chemistry
University of Tennessee
Knoxville, Tennessee 37996 (USA)
E-mail: xue@utk.edu

[b] *Z. Lu, Dr. M. Ozerov, Dr. D. Smirnov, S. M. Greer, Prof. S. Hill, Dr. J. Krzystek*
National High Magnetic Field Laboratory
Tallahassee, Florida 32310 (USA)
E-mail: krzystek@magnet.fsu.edu

[c] *Dr. Y. Cheng, Dr. L. L. Daemen*
Neutron Scattering Division
Oak Ridge National Laboratory
Oak Ridge, Tennessee 37831 (USA)

[d] *Prof. J. Telser*
Department of Biological, Physical and Chemical Sciences
Roosevelt University
Chicago, Illinois 60605 (USA)

[e] *Prof. K. Thirunavukkuarasu*
Department of Physics
Florida A&M University
Tallahassee, Florida 32307 (USA)

[f] *S. M. Greer*
Department of Chemistry & Biochemistry
Florida State University
Tallahassee, Florida 32306 (USA)

[g] *Prof. S. Hill*
Department of Physics
Florida State University
Tallahassee, Florida 32306 (USA)

[h] *Dr. K. Holldack*
Helmholtz-Zentrum Berlin für Materialien und Energie Gmbh
Institut für Methoden und Instrumente der Forschung mit Synchrotronstrahlung
12489 Berlin (Germany)

[i] *A. Aliabadi, Dr. A. Schnegg*
Helmholtz-Zentrum Berlin für Materialien und Energie GmbH
Institut für Nanospektroskopie, Berlin Joint EPR Laboratory
12489 Berlin (Germany)

[j] *Dr. A. Schnegg*
Max Planck Institute for Chemical Energy Conversion
45470 Mülheim an der Ruhr (Germany)

[k] *Prof. K. R. Dunbar*
Department of Chemistry
Texas A&M University
College Station, Texas 77842 (USA)

Supporting information for this article is available on the WWW under https://doi.org/10.1002/chem.202100705

Introduction

Single-molecule magnets (SMMs) exhibiting superparamagnetic behavior below a certain blocking temperature have potential applications in quantum computing (qubits), spintronics, and high-density storage devices.[1] Of particular interest are mononuclear SMMs, which consist of one metal center surrounded by organic ligands with slow magnetic relaxation. Hexacoordinated Co(II) complexes may derive their SMM behavior from unquenched orbital angular momentum.[2] In the case of quenched orbital angular momentum in paramagnetic compounds with spin $S \geq 1$, zero-field splitting (ZFS) of electronic states occurs as a result of second-order spin-orbit coupling (SOC).[1a–p,3] Large axial anisotropy and high energy barriers for magnetization reversal are among desired properties to extend magnetic relaxation times for these compounds. Typically, slow magnetic relaxation occurs in complexes with high magnetic anisotropy as indicated by a large, negative axial ZFS parameter, D, and a negligible rhombic ZFS parameter, E, resulting in a rhombicity, E/D, of around zero.[1n] One example of such SMMs is the tetra-coordinated Co(II) series, $Co(PPh_3)_2X_2$ (**Co-X**; X = Cl, **Co-Cl**; Br, **Co-Br**; I, **Co-I**; Figure 1).[4]

The ligand fields in **Co-X** lead to the high-spin electronic ground state $^4A_2$ of the d^7 Co(II) ions, which, with ZFS, splits into two levels, $m_S = \pm 1/2$ and $m_S = \pm 3/2$ (Figure 1). The energy difference between the two levels can be described by a spin-Hamiltonian (SH) in Eq. 1 which includes both ZFS and the Zeeman terms:

$$\hat{H}_S = D\left(\hat{S}_z^2 - \frac{5}{4}\right) + E\left(\hat{S}_x^2 - \hat{S}_y^2\right) + \mu_B g_x B_x \hat{S}_x + \mu_B g_y B_y \hat{S}_y + \mu_B g_z B_z \hat{S}_z \quad (1)$$

in which $\hat{S}$ = spin operator, μ_B = electron Bohr magneton, $g_{x,y,z}$ = g-tensor components, B = applied magnetic field.

The ZFS, typically given by the axial parameter, D, and the rhombic parameter, E in Eq. 1, is an important property of a metal complex, reflecting the ligand field encompassing the metal ion that affects the weak interaction of the unpaired electron spins mediated by the spin–orbit coupling.[1n,6] For many metal complexes, the magnitude of ZFS is too large in energy to be measured via conventional electron paramagnetic resonance (EPR) spectroscopy (X-band: 0.3 cm^{-1}; Q-band: 1.2 cm^{-1} based on the frequencies used in the bands). Thus, it is typically deduced indirectly from the effective g values or macroscopic methods such as magnetic susceptibility measurements or variable-temperature (VT), variable-field magnetic circular dichroism (VT-VH MCD).[4e,6d,7] HFEPR, which typically operates in the sub-THz frequency range, can directly determine ZFS in different metal complexes.[8] Of relevance here is an HFEPR study performed 55 years ago by van Stapele *et al.* on a complex related to **Co-X**, but homoleptic, Cs_3CoX_5 (X = Cl, Br), which contains tetragonally elongated $[CoX_4]^{2-}$.[9] These workers used 70 and 120 GHz radiation in combination with pulsed magnetic fields up to 9 T and found $D = -8.60$ cm^{-1} (X = Cl) and -10.68 cm^{-1} (X = Br).[9] Later, HFEPR with swept fields was used to study **Co-Cl**, yielding its D, E, and g (g_x, g_y, g_z) values (Table 1).[4d] More recently, Lu, Nelson, and coworkers demonstrated the use of terahertz time-domain EPR through a simple tabletop approach to probe the transitions between the spin levels in **Co-Cl** and **Co-Br**,[4f] yielding the spin-Hamiltonian parameters: $D = -14.76$, $E = 1.61$ cm^{-1} for **Co-Cl** and $D = -13.90$, $E = 0.96$ cm^{-1} for **Co-Br** along with g (g_x, g_y, g_z) values (Table 1). Magnetometry has also been used to indirectly determine D and E values of the three **Co-X** complexes: $D = -11.6$, $E = 2.43$ cm^{-1} for **Co-Cl**,[10] $D = -12.5$, $|E| = 0.70$ cm^{-1} for **Co-Br**,[10] and $D = -36.9$ cm^{-1} for **Co-I**[4a] along with some of the g values.

In addition to the spin-Hamiltonian parameters (Eq. 1), representing essentially electronic-only properties, there are other important nuclear-related, vibrational (or phonon) properties in SMM solids. Spin–phonon coupling does play a critical role in magnetic relaxation in metal complexes, including SMMs and potential qubits.[1a–g,11] However, understanding of these interactions, including direct observation of the coupling and determination of the coupling magnitudes, is limited. There have, however, been recent studies to understand how spin-phonon couplings lead to relaxation.[12] Despite these efforts, there are fairly few direct observations of spin-phonon

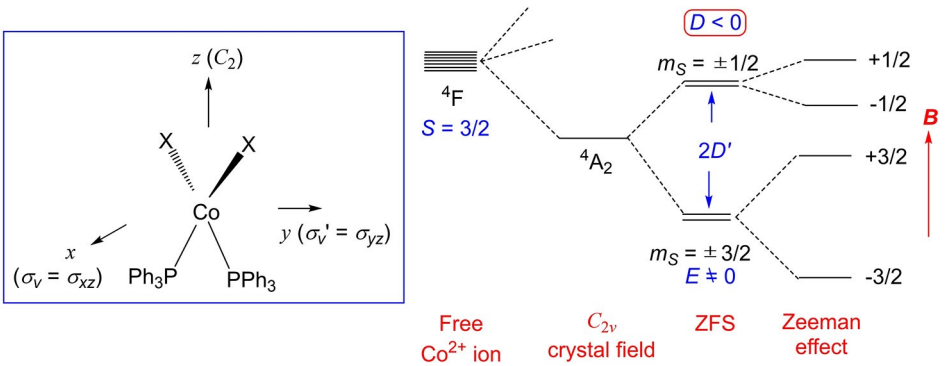

Figure 1. (Left) Diagram of $Co(PPh_3)_2X_2$ (**Co-X**; X = Cl, **Co-Cl**; Br, **Co-Br**; I, **Co-I**). (Right) Spin level diagram of the complexes in the case of $D < 0$. $D' = (D^2 + 3E^2)^{1/2}$. It should be pointed out that the $m_S = \pm 1/2$ and $m_S = \pm 3/2$ are nominal labels for the levels, as the zero-field $|\pm 1/2\rangle$ and $|\pm 3/2\rangle$ levels are mixed when $E \neq 0$, as found for **Co-X**.[5] For excited electronic states of the complexes involved in second-order SOC, contributing to ZFS, see Figure 2.

Table 1. Spin-Hamiltonian parameters for **Co-Cl**, **Co-Br**, and **Co-I**.

Complex	Method	D (cm^{-1})	$\lvert E\rvert$ (cm^{-1})[b]	$\lvert E/D\rvert$	$D'=(D^2+3E^2)^{1/2}$ (cm^{-1})	g_x	g_y	g_z	Ref.
Co-Cl	Variable-field INS				14.9(2)				Current work
	VT INS				14.7(2)				Current work
	FIRMS				14.93(13)				Current work
	FD-FT THz-EPR				14.97(5)	2.3	2.3	2.15	Current work
	THz time-domain EPR	−14.76	1.61	0.109	15.0	2.20	2.18	2.23	[4f]
	HFEPR	−14.76(2)	1.141(8)	0.0773(5)	14.89(2)	2.166(4)	2.170(4)	2.240(5)	[4d], Current work
	MCD	−14(3)	0.96(20)	0.08(2)	14(3)	2.15(5)	2.16(4)	2.17(3)	[4d]
	Magnetometry	−11.6	2.43	0.21	12.3	2.215		2.265	[10]
	Calculated[a]				14.91				Current work
Co-Br	VT-INS				13.8(6)				Current work
	FIRMS				13.81(11)				Current work
	FD-FT THz-EPR				13.75(5)	2.3	2.3	2.13	Current work
	THz time-domain EPR	−13.90	0.96	0.069	14.0	2.10	2.10	2.22	[4f]
	HFEPR	−13.82(2)	0.29(1)	0.02	13.83(2)	2.24(1)	2.15(1)	2.24(2)	Current work
	Magnetometry	−12.5	0.70	0.056	12.6	2.006		2.164	[10]
	Calculated[a]				13.86				Current work
Co-I	VT-INS				13.7(3)				Current work
	FIRMS				13.69(15)				Current work
	FD-FT THz-EPR				13.6(1)	2.2(1)	2.2(1)	2.0(1)	Current work
	HFEPR	−13.13(10)	2.11(5)	0.16	13.63(10)	2.28(4)	–	2.36(2)	Current work
	Magnetometry	−36.9							[4a]
	Calculated[a]				13.63				Current work

[a] LFT does not provide separate D and E components, only the splitting of the ground state spin quartet into two doublets (or levels). Half of this splitting is what is provided. Calculated g_{eff} values indicate a negative sign of ZFS. The parameters in Table S6 were used, with $\zeta=459$ cm^{-1} (**Co-Cl**), $\zeta=338$ cm^{-1} (**Co-Br**), and $\zeta=355$ cm^{-1} (**Co-I**). [b] Sign of E values in cited references is positive. The sign was not determined in the current work. Absolute signs are placed to all values here.

couplings in paramagnetic systems.[13] It should be pointed out that phonons of molecular crystals include both internal and external modes.[13c,14] Internal modes, also known as intramolecular or molecular vibrations, involve significant distortions of atoms that comprise a part of the molecule with a small displacement of the molecular center-of-mass. In external modes, also called lattice vibrations, the molecules vibrate primarily as a whole with little internal distortion. However, all modes in a molecular crystal essentially exhibit both features to different extent (as demonstrated in the movies in the Supporting Information discussed below) and, from the perspectives of solid-state physics, all modes originate from the same governing equations and have unified mathematical representations.[15] In other words, phonons describe the collective vibrations of all atoms in the solid crystal (a periodic tessellation of the unit cell). Thus, the internal and external modes are not distinguished in the current work, and they are both called phonons. AC susceptibility studies of **Co-Cl**,[4b] **Co-Br**,[4c] and **Co-I**[4a] showed their slow magnetic relaxation in the presence of DC magnetic fields. For **Co-Cl**, the lack of slow relaxation in the absence of the DC field was attributed to quantum tunneling of the magnetization (QTM).[4b] In **Co-Br**, two relaxation processes, one thermal activation (Orbach) and the other a direct or Raman process, were observed.[4c] In **Co-I**, studies pointed to the Orbach process in the relaxation.[4a]

There are several experimental techniques to simultaneously probe magnetic transitions and spin-phonon coupling in molecular complexes. Far-IR, Raman, and INS spectroscopies have been used in the present study and are thus briefly introduced. Far-IR is obvious to probe low-energy IR-active phonon excitations. In addition, transitions between levels from ZFS, which are magnetic-dipole-allowed by symmetry and selection rules ($\Delta m_S=0, \pm1$), can be observed in far-IR.[16] Thus, the technique in varying external magnetic fields (in contrast to continuous-wave EPR, where the frequency is fixed and the magnetic field is swept) has been used to view magnetic transitions in metal complexes.[1d,13a,b,16,17] Magnetic transitions and those of IR-active phonons may undergo spin-phonon coupling, which is revealed in the far-IR region.[13a,17d] In this work, two far-IR setups with applied magnetic fields have been used, which differ in their technical outline and specifications. The two setups are called far-infrared magnetic spectroscopy (FIRMS)[13a,b,17a,c–j] and frequency-domain Fourier-transform terahertz EPR (FD-FT THz-EPR).[17k,l,18] Raman spectroscopy is another technique to probe low-energy, Raman-active phonon excitations. The magnetic transitions between ZFS levels are vanishingly weak in Raman.[13b] However, these magnetic transitions may undergo spin-phonon coupling with Raman-active phonons.[13b] This interaction imparts both spin and phonon features to the coupled peaks, leading to observation of the coupled peaks in Raman spectra in varying external magnetic fields. This technique is called magneto-Raman spectroscopy, as some of us have recently reported for $Co(acac)_2(H_2O)_2$ and isotopologues.[13b] Magnetic transitions in $[Fe(H_2O)_6]SiF_6$ were directly observed in magneto-Raman 30 years ago by Gnezdilov and coworkers,[1d,19] likely as a result of the presence of a large

orbital angular momentum contribution to the magnetic levels of the $3d^6$ $[Fe(H_2O)_6]^{2+}$ ion with its nearly O_h ligand field.[19,20]

INS[21] has also been used to study magnetic[22] and phonon[23] excitations in metal complexes. The incident neutrons, as particles with $I = 1/2$, are scattered by nuclei of atoms in a sample, leading to phonon excitations. In addition, the neutron magnetic moment interacts with the magnetic field of the sample (created by unpaired electrons), leading to magnetic transitions.[22] A schematic representation of the INS process and the cross section of magnetic scattering for spin-only neutron scattering is given in the Supporting Information (Section S2). Neutron instruments for coordination chemistry studies have been recently reviewed,[22e] but the several experimental methods typically employed to identify a peak of magnetic transition in INS spectra of metal complexes warrant a brief summary below: (1) Use of a direct-geometry INS spectrometer to measure the dependence of peak intensity vs. neutron scattering angle at a given temperature.[13c,22b,e,24] This is a unique feature of INS, as peak intensities of magnetic transitions fall off with increasing scattering angle as a result of a decrease in the magnetic form factors,[21] while intensities of phonon peaks increase with increasing scattering angle. (2) VT INS, as electrons and phonons are fermions and bosons, respectively, leading to different temperature dependence of magnetic and phonon peaks in so-called Bose-corrected VT INS spectra.[13c,d,17d,22b,24,25] (3) Variable-magnetic-field INS conducted with an external magnet, leading to the shifts of Zeeman-split magnetic transitions with fields.[13c,d,17d,24c] This technique often unambiguously identifies the magnetic resonance in INS spectra, but is technically challenging.[17d,24c]

Phonon characterization, including DFT phonon calculations,[17c] is important for understanding spin-phonon coupling in molecular complexes. In electromagnetic far-IR and Raman spectroscopies, whether phonon excitations are observed depends on symmetry-based selection rules. In contrast, INS, based on kinetic energy transfer, does not have symmetry-based selection rules.[23] That is, all phonon modes are observable in INS spectra. Calculations using the VASP and phonopy programs[26] give phonon energies, their symmetries and calculated INS spectra to compare with the experimental INS spectra.[13b,d,17d] In addition, the calculations yield spin densities on all atoms of a metal complex.[1r]

The goal of the current work is to directly probe spin-phonon couplings in **Co-X** (X = Cl, Br, I), including the magnitudes of the couplings, and provide comprehensive spectroscopic and theoretical studies of the phonon properties of the complexes, including their symmetries and energies. We also aim to obtain visual depictions of the phonons undergoing the spin-phonon couplings. Probing spin-phonon couplings requires precise determination of energies of the magnetic excited levels (i.e., ZFS between the $m_S = \pm 3/2$ ground and $m_S = \pm 1/2$ excited levels) in the **Co-X** complexes. LFT studies in the current work, as well as previous quantum chemical theory (QCT) studies[4g] on a truncated model for **Co-Cl**, have revealed the source of magnetic anisotropy and calculated accurately the ZFS parameters D' in the three **Co-X** complexes. The DFT calculations have also yielded spin densities on the atoms in **Co-X**, showing that the higher the spin density on the Co atom, larger the D' parameter of the compound.

Results and Discussion

LFT background of the Co-X series (X = Cl, Br, I)

As is typical for roughly tetrahedral open-shell complexes, electronic absorption spectra of the **Co-X** (X = Cl, Br, I) series are rich and informative, and the complete series was thoroughly studied many years ago. For **Co-Cl**, Simo and Holt provided a comprehensive analysis of the single-crystal electronic absorption of Co-doped $Zn(PPh_3)_2Cl_2$ (**Co/Zn-Cl**).[27] Tomlinson *et al.* did the same for Co-doped $Zn(PPh_3)_2Br_2$ (**Co/Zn-Br**) and $Zn(PPh_3)_2I_2$ (**Co/Zn-I**).[28] In **Co-X** with C_{2v} point group symmetry, the molecular z axis lies along the C_2 axis (i.e., bisecting the X–Co–X and P–Co–P bond angles as shown in Figure 1), the x axis lies in the X–Co–X plane (σ_v), and the y axis lies in the P–Co–P plane (σ_v'). The spectroscopic results are summarized in Table S4 in Supporting Information, which corrects a minor discrepancy between the analysis described by Tomlinson *et al.* and data in a table in their paper.[28] In C_{2v} point group symmetry, the ground electronic state of **Co-X** is $^4A_2$, derived from the parent $^4A_2$(F) term in T_d symmetry ($e^4t_2^3$ in strong-field notation). The quartet excited states are $^4T_2$(F) ($e^3t_2^4$), $^4T_1$(F) ($e^2t_2^5$), and $^4T_1$(P) ($e^3t_2^4$) in T_d symmetry and each splits into $^4A_1$ (for $^4T_2$) or $^4A_2$ (for $^4T_1$), $^4B_1$, and $^4B_2$ states. The electronic transition $^4A_2 \rightarrow {}^4A_1$ is symmetry forbidden, but $^4A_2 \rightarrow {}^4A_2$ is allowed with z polarization, $^4A_2 \rightarrow {}^4B_1$ is allowed with y polarization, and $^4A_2 \rightarrow {}^4B_2$ is allowed with x polarization. Transitions to the states derived from $^4T_2$ would be in the mid-IR region and thus very difficult, although not impossible,[9,29] to observe. Transitions to those derived from $^4T_1$(F,P) are in the visible region and all were observed experimentally with their polarization assignments.[27,28] These states are given in Figure 2, which also shows the descent in symmetry for a Co(II) from the free-ion to a hypothetical, tetrahedral $[CoX_4]^{2-}$ complex,[30] to a hypothetical tetragonally compressed $[CoX_4]^{2-}$ complex, to the $CoX_2(PPh_3)_2$ system which has C_{2v} symmetry.

These results can then be used with a LFT analysis using the Angular Overlap Model (AOM) to provide a quantitative comparison among the three complexes. The above geometrical model is employed, with the experimental bond angles ∠X–Co–X and ∠P–Co–P in each case, as given in Table S5.

The experimental data were satisfactorily fitted using the AOM (Table S4). As simplifying assumptions, the two halide ligands and the two phosphine ligands were held equivalent. Both ligand types were constrained to have cylindrical π-interactions: donating for X and accepting for P. The fit values for **Co-Cl** and **Co-Br** can be compared to those determined by Davies *et al.*,[31] who used single-crystal magnetic susceptibility data in combination with the same literature electronic absorption data as was used here. As shown in Table S6, the two analyses are in reasonable agreement, the chief difference being that in the present work the π-acidity of the PPh_3 ligands is proposed to be greater. As also evident in Table S6, the σ-

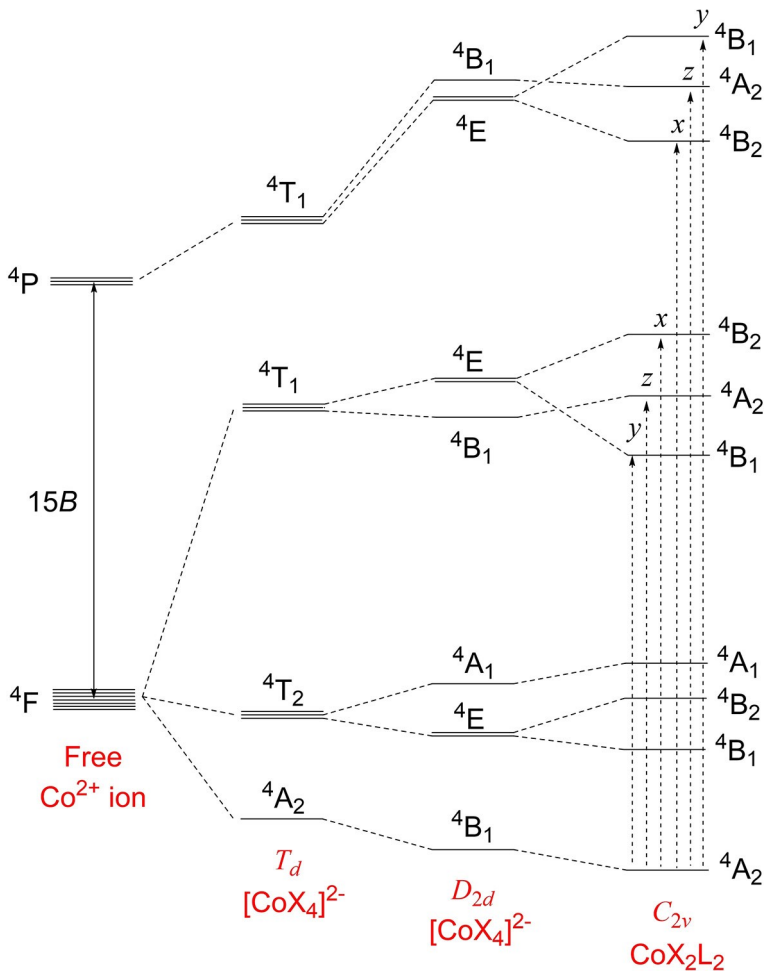

Figure 2. Electronic quartet states of $3d^7$ Co(II) as a free-ion, in a tetrahedral (T_d) ligand field, in a tetragonally compressed ligand field (D_{2d}), and in a rhombic (C_{2v}) ligand field as in **Co-X**. This figure is based on one derived for Ni(II) ($3d^8$) as in $NiX_2(PPh_3)_2$.[8b] The electronic transitions are also indicated, together with their polarization, fully for the C_{2v} case,[28] and partially for the D_{2d} case, which is relevant to the discussion of previous work.[6c,9] Inclusion of spin-orbit coupling (not shown) would split each of the quartets into two degenerate levels, affording the observed ZFS. This effect is shown graphically in Figure 3e of the paper by Sundararajan *et al.*[4g] and in tabular format in Tables S7b, S8b, S9b, S10, and S11 in the Supporting Information.

and π-donor strength of the halide ligands in **Co-X** decreases in the order $Cl^- > Br^- > I^-$, in agreement with the spectrochemical series.[32] The values determined here, and previously,[31] for the Racah interelectronic repulsion parameter B are ~60% of the free-ion value,[33] which is plausible for a highly covalent compound. The complete output listing of the electronic states and orbital descriptions (using the Ligfield software[34]) for each of the **Co-X** series is given in Tables S7–S9 (Supporting Information).

It can be seen there that inclusion of the Racah C parameter, so that $C/B = 4.26$, the free-ion ratio,[33] gives a plethora of doublet excited states well above the quartet states, but there are relatively lower lying doublet states in the ranges of 9500–12500 cm^{-1} and 14000–17500 cm^{-1} above the ground state [i.e., close to quartet states derived from $^4T_1$(F,P)]. These doublet excited states might contribute to ZFS (see below) and possibly to the observed absorption bands. For a more tractable depiction of the doublet states, Table S12 gives the complete d^7 electronic states for a hypothetical $[CoX_4]^{2-}$ ion with ideal T_d symmetry.

Experimental studies of magnetic excitations in Co-X

INS: For **Co-Cl**, both variable-field (with a 10 T magnet) and VT INS studies were conducted. The former gave spectra in Figure 3-Left with low signal-to-noise ratio of the peaks, because the magnet blocked many detectors. A comparison of the spectra at 0 and 10 T shows that the peak at 29.7(2) cm^{-1} at 0 T disappears at 10 T, indicating its magnetic nature [i.e., $2D' =$ 29.7(2) cm^{-1}]. VT INS spectra of **Co-Cl** at 5, 30, 60 and 90 K are presented in Figure 3-Right. At zero applied field, only one magnetic transition from the $m_S = \pm 3/2$ ground level to the $m_S = \pm 1/2$ excited level is expected in the INS spectra. After Bose-correction of the VT INS spectra to make the intensities of phonon peaks relatively constant, the intensity of the magnetic transition should decrease with increasing temperature, as the

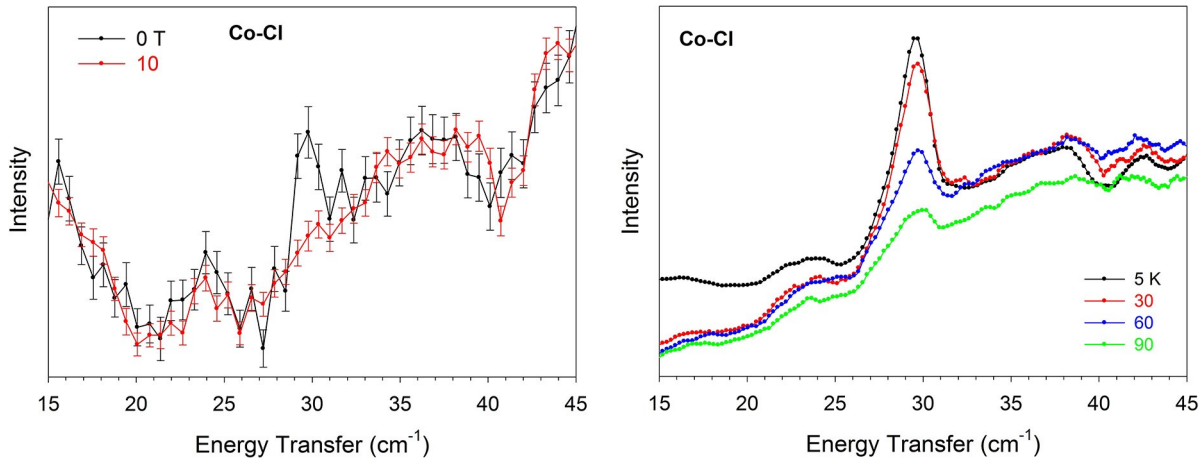

Figure 3. Co-Cl: (Left) Variable-field INS spectra at DCS at 1.5–1.6 K; (Right) Bose-corrected forward-scattering VT INS spectra at VISION. Figure S20 in the Supporting Information shows additional VT INS spectra of **Co-Cl**, revealing phonon excitations and their symmetry assignments.

$m_S = \pm 1/2$ excited level is increasingly thermally populated at the expense of the $m_S = \pm 3/2$ ground level. Figure 3-Right shows that the magnetic transition at 5 K by VT INS is at $2D' = 29.5(2)$ cm^{-1}. The sign of the D parameter, as those of **Co-Br** and **Co-I** below, was based on the HFEPR results, as the INS results cannot determine the sign.

For **Co-Br and Co-I**, VT INS studies were similarly conducted and the spectra are given in Figure S20-Top and -Bottom, respectively. Magnetic transitions of **Co-Br** and **Co-I** are clearly observed at $2D' = 27.6(4)$ cm^{-1} and 27.3(0.3) cm^{-1}, respectively.

FIRMS: Magnetic transitions (at 0 T) between the two ZFS sublevels (e.g., $m_S = -3/2 \rightarrow -1/2$ and $m_S = +3/2 \rightarrow +1/2$) in **Co-X** are magnetic-dipole-allowed by symmetry and selection rules ($\Delta m_S = 0, \pm 1$).[16] In C_{2v} local symmetry around the Co(II) ion, the magnetic dipole moment operators have B_2, B_1 and A_2 symmetries as the rotations R_x, R_y and R_z, respectively. In the double group C_{2v}', both $m_S = \pm 3/2$ and $\pm 1/2$ levels are represented by $E_{1/2}$.[35] Thus, the magnetic transitions are observable in far-IR. Frequency-domain spectroscopy (i.e., FIRMS) using high magnetic fields, revealing how the Zeeman effect changes the transitions between ZFS levels, is ideal to probe magnetic transitions in addition to studying IR-active phonon excitations.[13a,b,16,17c–m,36] In the present $S = 3/2$, $D < 0$ case, the $m_S = \pm 3/2$ level can be excited to the $m_S = \pm 1/2$ level and spin-Hamiltonian parameters can then be extracted from the spectra.

Transmittance of **Co-Cl**, **Co-Br**, and **Co-I** at 0 and 17 T in Figure 4 reveals the changes caused by the external magnetic fields with additional FIRMS spectra and assignments of phonon symmetries for **Co-Cl** and **Co-Br** in Figures S1–S3. Transmission spectra normalized by the average are shown as a function of magnetic fields in Figure 5. The largest transmission changes are presented in blue color and are proportional to the intensity of the transitions between the levels split in magnetic field, while the yellow color corresponds to regions lacking magnetic-dependent spectral features. The magnetic resonance absorption is most intense at 0 T, allowing *direct* determination of the energy gap between the $\pm 3/2$ and $\pm 1/2$ level from FIRMS spectra as follows: **Co-Cl**, 29.85(13) cm^{-1}; **Co-Br**, 27.62(11) cm^{-1}; and **Co-I**, 27.38(15) cm^{-1} (Figure 5). The intensity of the magnetic absorption decreases and spreads out in high magnetic fields, because the intensity and frequency of the

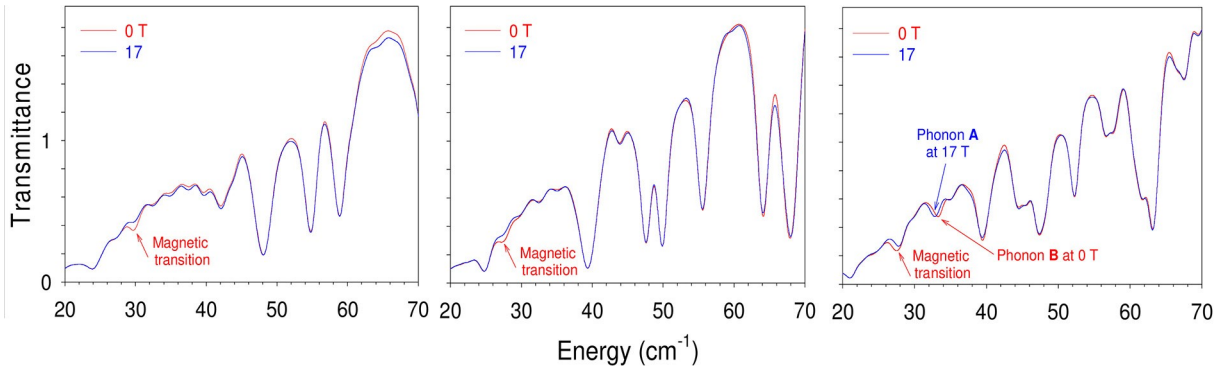

Figure 4. FIRMS spectra of the complexes at 5 K and 0 and 17 T: (Left) **Co-Cl**, (Middle) **Co-Br**, (Right) **Co-I**. Assignments of the phonon peaks in **Co-Cl** and **Co-Br** are given in Figures S1–S2. The phonons in **Co-I** could not be assigned.

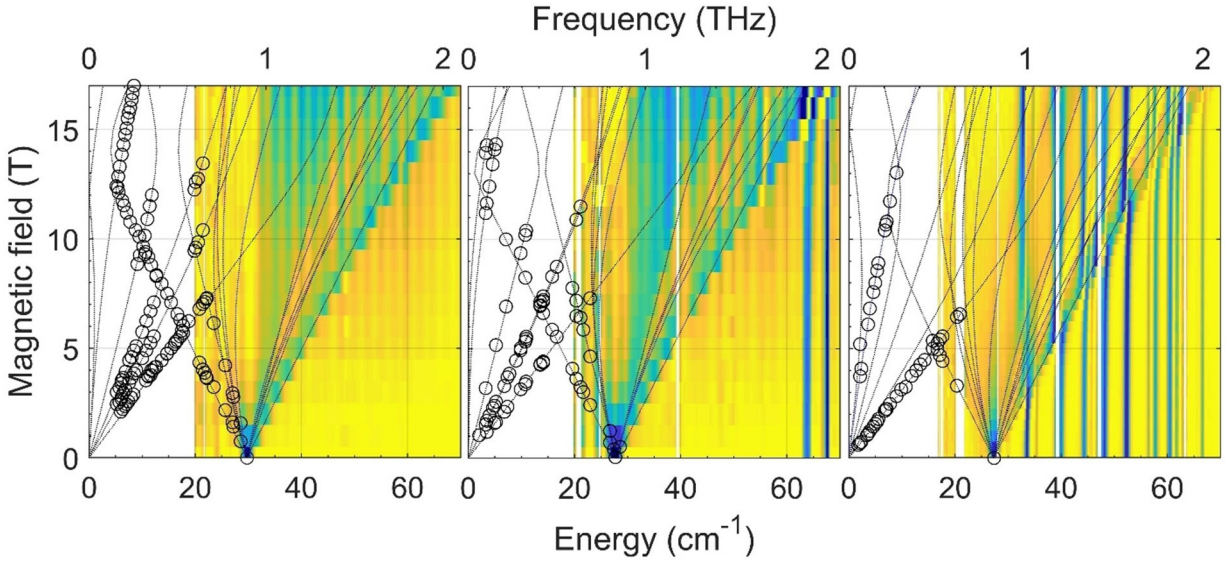

Figure 5. FIRMS maps (normalized transmission vs. field and energy/frequency): (Left) **Co-Cl**, (Middle) **Co-Br**, (Right) **Co-I** with HFEPR results superimposed. The color trend from blue to yellow corresponds to a decrease of the magnetic absorption. The lines are simulations of turning points in the powder spectra that assume the (best-fitted) spin-Hamiltonian parameters in Table 1. The circles correspond to the observed HFEPR resonances, except for the zero-field resonance in **Co-I** obtained from FIRMS spectra. The equidistant vertical stripes are due to instrumental artifacts, while the white regions correspond to spectral ranges without reliable data. Spin-phonon couplings in the FIRMS plots normalized by average are presented below in Figures 7–8.

transitions are defined by the direction of the magnetic field relative to the magnetic anisotropy ***D***- and ***g***-tensors using microcrystalline samples with random orientations. The black lines in Figure 5 show *calculated* field dependences of turning points[37] in the powder spectra. While the low-energy turning points are revealed in HFEPR spectra (shown as circles in Figure 5), turning points with energies larger than $2D'$ show up in FIRMS maps (black lines). The maps are consistent with $D<0$, and these results are in excellent agreement with calculated powder spectra of magnetic absorption (Figure S4) using the spin-Hamiltonian parameters from HFEPR in Table 1, thus confirming the HFEPR determination of the parameters. One additional finding from Figure 4-Right is that, for **Co-I**, the phonon at 33.3(1) cm^{-1} (phonon **B** in Figure 8-Right and Table 2 below) is coupled to the magnetic transition even at 0 T, pushing each other apart. At 17 T, when the magnetic transition (peak **A** in Figure 8-Right) is shifted away after several avoided crossings, it is no longer coupled to this phonon. In fact, the original peak of magnetic transition, **A**, has become the phonon (through the coupling during the avoided crossing with **B**) and now "returned" to a new position (at 32.8 cm^{-1} to the left of the original position of **B** at 0 T).

Magneto-Raman spectra of **Co-Cl, Co-Br**, and **Co-I** under 0–14 T magnetic fields (Figures S5, S6 and S7, Supporting Information) do not reveal the magnetic transitions in these complexes. Phonon features of the Raman spectra of **Co-X** at 0 T are discussed below.

FD-FT THz-EPR: Figure 6 depicts FD-FT THz-EPR of **Co-X** at 0–7 T with a spectral resolution of 0.5 cm^{-1}. Division by a reference spectrum measured under identical conditions, but with a field offset, leads to FD-FT THz-EPR magnetic-field-division spectra (MDS, details in Section S5, Supporting Information) containing only the field-dependent components of the spectrum. Magnetic resonances in MDS are similar to those in

Table 2. Energies of phonons involved in spin-phonon couplings and the coupling constants.

Co-Cl Phonon	B	C	D	E					
Phonon peak (cm^{-1})	42.2(1)	48.1(3)	54.8(2)	58.9(3)					
A (cm^{-1})	1.3(2)	1.3(1)	1.3(2)	1.4(3)					
Co-Br Phonon	B	C	D	E	F	G			
Phonon peak (cm^{-1})	39.5(3)	47.5(1)	50.0(1)	55.6(2)	64.0(2)	68.1(2)			
A (cm^{-1})	1.0(3)	1.3(4)	1.1(3)	1.5(3)	1.4(4)	1.8(4)			
Co-I Phonon	B	C	D	E	F	G	H	I	J
Phonon peak (cm^{-1})	33.3(1)	35.3(1)	39.5(2)	44.1(1)	47.7(2)	52.3(2)	56.7(1)	61.0(2)	63.0(1)
A (cm^{-1})	1.3(2)	0.9(3)	1.5(3)	1.6(2)	1.8(2)	1.6(3)	1.8(3)	2.0(4)	1.1(3)

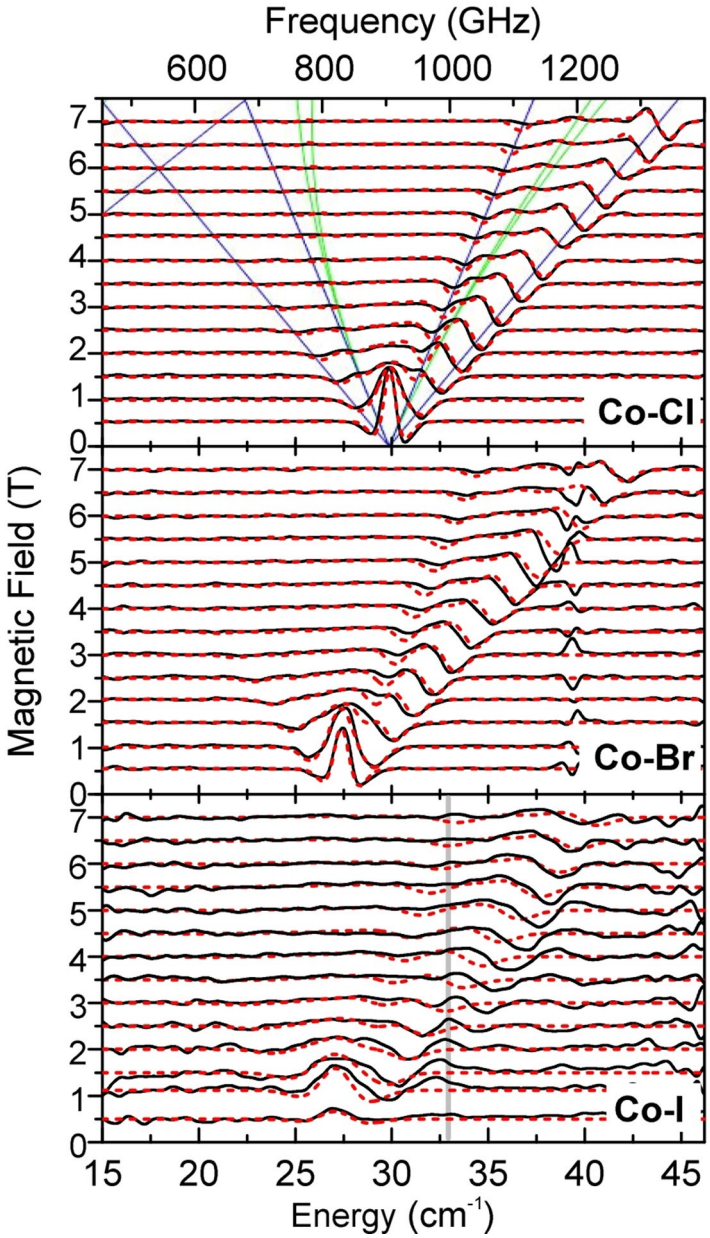

Figure 6. FD-FT THz-EPR MDS at 5 K: (Top) **Co-Cl**, (Middle) **Co-Br**, (Bottom) **Co-I**. Spectra are plotted as offset to corresponding magnetic field. Experimental spectra (black) are overlaid on spin-only simulations (dashed red; simulation parameters in Table 1). In the top panel, simulated transition energies for magnetic fields parallel (blue) and perpendicular (green) to the z-axis of the ZFS tensor are shown. The grey shaded bar in the lower panel marks the transition energy of a phonon at 33 cm^{-1}.

first-derivative EPR spectra. Field-independent phonons are cancelled by this technique. However, in the case of spin-phonon couplings, phonons shift in an applied magnetic field and therefore lead to peaks of magnetic transitions similar to EPR resonances. Discrimination between magnetic transitions originating from EPR resonances and spin-phonon coupled peaks requires the comparison with simulated spectra using the spin-Hamiltonian in Eq. 1. In Figure 6, EPR spectra simulated with Eq. 1 are plotted alongside measured spectra. Field *vs.* frequency plots in Figure 6 are equivalent to Figure 5, but allow for a more convenient comparison of measured and simulated spectra.

The simulations were performed with the *EasySpin* program and its extensions for frequency-domain EPR.[17k] Very good estimates of $2D'$ can be directly obtained from the zero-field FD-FT THz-EPR spectrum. However, more accurate D' and g values are available from simulations of MDS at different external magnetic fields, giving the SH parameters for **Co-X** in Table 1. Simulations of the spectra can also provide estimates of E. However, these values are usually less accurate than those

from HFEPR.[38] Thus, the *E* parameters from FD-FT THz-EPR are not given in Table 1.

A very good match between experiment and simulation was achieved for **Co-Cl**. No indication of spin-phonon coupling is found in the spectral window. Similarly, good agreement was found for **Co-Br**. However, a distortion around 39.5 cm^{-1} is observed, originating from a strong (phonon) absorption (see Figures 4 and S11 for a view of the phonon). For MDS spectra of **Co-Br** between 5.5 T and 6.5 T, a partial overlap with this absorption leads to a deviation of the simulated and measured spectrum. However, despite the high quality of the data, no clear assignment of spin-phonon coupling is possible in this case. Interestingly, spectra of both **Co-Cl** and **Co-Br** show low-energy phonon modes at ~25 cm^{-1}, which are very close to the zero-field EPR peaks (see Figure 4). Yet, neither of these modes appears to couple to the magnetic resonance (or the coupling is too weak to be observed here), when they overlap with the magnetic transitions at elevated fields, and therefore does not alter the MDS of **Co-Cl** and **Co-Br**.

Spectra of **Co-I**, on the contrary, show pronounced spin-phonon coupling between 2.5 T and 5.5 T, leading to clear deviations between experimental and calculated MDS [see dashed spectra in Figure 6-Bottom simulated with Eq. 1 (without spin-phonon coupling)]. While experimental spectra and simulations match very well below 2 T and above 5.5 T, spectra in the intermediate field range exhibit an additional splitting, which is not reproduced by the SH simulations. The splitting of the magnetic resonance by spin-phonon coupling is most obvious in the 3 T MDS of **Co-I**, where the predicted magnetic resonance (without spin phonon coupling) overlaps with the phonon at 33 cm^{-1} (phonon **B** in Figure 8-Right and Table 2), as discussed earlier in Figure 4-Right. The experimental MDS clearly reveals two minima centered around 33 cm^{-1}, which originate from an avoided crossing of the Co(II) spin resonance and phonon **B**.

HFEPR. Co-Cl was the subject of an earlier detailed HFEPR and MCD study by some of us.[4d] In the current work, we have confirmed the previous results and added spectra at several high frequencies to the 2-D field vs. frequency map of turning points[37] (Figure 5-Left and Figure S13-Top), which were unavailable earlier.[4d] One such spectrum, obtained at 815 GHz, which is just below the frequency (~890 GHz) of the transition between the $m_S = \pm 3/2$ and $m_S = \pm 1/2$ levels as determined at zero field by FIRMS and FD-FT THz-EPR, is shown in Figure S14.

Co-Br generated a very good HFEPR response, similarly to **Co-Cl**. Three representative HFEPR spectra (Figures S15, S16 and S17) are shown in Supporting Information. Figure S15 gives an optically modulated spectrum recorded at the frequency corresponding almost exactly to the zero-field transition frequency (~830 GHz) between the $m_S = \pm 3/2$ and $m_S = \pm 1/2$ levels. Figure S16 shows a conventional, magnetically modulated spectrum at 473 GHz, while Figure S17 displays a spectrum at a low frequency of 98 GHz, where it is possible to observe all three turning points of the intra-Kramers m_S=-3/2→ +3/2 transition. The full 2-D map of HFEPR turning points in **Co-Br** is shown in Figure 6-Middle and Figure S13-Middle.

The HFEPR response of **Co-I** was weaker than those of the two other congeners. In particular, most of the observed resonances originated from the intra-Kramers $m_S = -3/2 \rightarrow +3/2$ transition within the $m_S = \pm 3/2$ doublet. Only in one narrow frequency region (ca. 500 GHz) were we able to record resonances belonging to the inter-Kramers $m_S = -3/2 \rightarrow +1/2$ transition, which are informative with regard to ZFS (Figure S18). Figure S19 shows a spectrum at the low end of available frequencies (63 GHz) which turned out to be the only frequency at which we were able to observe all three turning points of the intra-Kramers $m_S = -3/2 \rightarrow +3/2$ transition. As a result, a least-square fit to the 2-D field vs. frequency map (Figure 5-Right and Figure S13-Bottom) yielded lower accuracy in the spin-Hamiltonian parameters for **Co-I** than those for **Co-Cl** and **Co-Br**.

Least-square fits of the Hamiltonian parameters to the 2-D field vs. frequency maps for the three complexes resulted in the following values: $D = -14.76(2)$, $|E| = 1.141(8)$ cm^{-1} for **Co-Cl**, $D = -13.82(2)$, $|E| = 0.29(1)$ cm^{-1} for **Co-Br**, and $D = -13.13(10)$, $|E| = 2.11(5)$ cm^{-1} for **Co-I**, along with most g (g_x, g_y, g_z) values listed in Table 1.

Analysis of ZFS in Co-X by ligand-field theory

Spin-orbit coupling can be included into the above LFT-AOM analysis to reproduce experimental ZFS parameters (Table S11). Davies *et al.* used $\zeta = 500$ cm^{-1}, which is only slightly lower than the free-ion value (533 cm^{-1}).[39] We find that, for **Co-Cl**, use of $\zeta = 459$ cm^{-1} (86% of the free-ion value, perhaps more realistic than 94% used earlier) exactly reproduces the experimental ZFS parameters (Table 1 in comparison to those from HFEPR). It is not possible to deconvolute this splitting into D and E components, nor to their sign. The spin expectation value of each of the levels of the ground state quartet does not readily afford the spin-only values of $m_S = \pm 1/2$, $\pm 3/2$ (Tables S7b, S8b, S9b, S10, and S11), e.g., for **Co-Cl**, $m_S = \pm 0.14$ and $m_S = \pm 0.85$ (Table S7b). However, inclusion of an applied field [300 mT, as in conventional, X-band EPR; using the locally written (J. Telser) program DDN] sheds light on this situation, as shown for the electronic states of the lowest spin quartet state for a hypothetical $[CoX_4]^{2-}$ ion with D_{2d} symmetry (Table S10) and for the real **Co-X** complexes with C_{2v} symmetry (Table S11). These cases give observed g_{eff} values for **Co-Cl** as follows: $g_{x(max)} = 6.96$, $g_{y(min)} = 0.57$, $g_{z(mid)} = 0.91$ (Table S11a). The assignment to x, y, and z components of $\boldsymbol{g}_{eff}$ is a consequence of the chosen AOM coordinate system, but in general for $S = 3/2$, observed g_{eff} values in which one is large and two are very small (for intrinsic $g = 2.00$, $\boldsymbol{g}_{eff} = [6, 0, 0]$[40]) are characteristic of $D < 0$, as is the case for **Co-Cl**.[41] Smaller values of ζ (~65% of the free-ion value; See Table 1) exactly reproduce the experimental ZFS for **Co-Br** and **Co-I**, again with negative sign, as demonstrated by their $\boldsymbol{g}_{eff}$ components (Tables S11b and S11c, respectively). The origin of the ZFS in **Co-X** is discussed in the Supporting Information.

Experimental and calculated phonon spectra and studies of spin-phonon couplings

Crystals of **Co-Cl** [*P*2/*c*, No. 13, 293(2) and 295 K],[4b,e] **Co-Br** (*P*2/*c*, 295 K),[4e] and **Co-I** [$P2_1/c$, No. 14, 110(2) K][4a] in the current work are all monoclinic with C_{2h} crystallographic lattice symmetry. Thus, phonon modes of their crystalline solids have one of the four symmetries: A_g, B_g, A_u, and B_u.[42] Phonons of the A_u and B_u modes are IR-active, while those of the A_g and B_g modes are Raman-active.

Phonon modes of the three complexes, energies of the modes, and INS spectra were obtained by the VASP and phonopy calculations.[26] Spin-phonon coupling simulations were conducted for the avoided crossings in FIRMS spectra using Hamiltonians in Eqs. 5 and 7 below.

Phonon excitations in INS, FIRMS and Raman spectra, calculated INS spectra, and computations of phonon excitations and symmetries: Accurate phonon calculations are a critical step to understand the atomic displacements leading to spin-phonon coupling in SMMs. In the most general sense, the atomic displacement pattern associated with a specific vibrational mode can change the bond length and angle, resulting in changes of electronic and magnetic structure. Different vibrational modes at different frequencies can affect the electronic and magnetic structure differently. The DFT phonon calculations of the INS spectra were conducted using the reported single-crystal structures of the three complexes (Table S5) with two goals: (1) Determine the symmetries of phonon modes and their energies; (2) Give calculated INS spectra to compare with the experimental ones. The lattice symmetry for all three crystal structures is C_{2h}, which was used to assign symmetries to each phonon mode. The calculated phonon modes and their energies for **Co-Cl**, **Co-Br**, and **Co-I** are given in Tables S1–S3. In addition, the DFT calculations gave calculated INS spectra in Figures S21, S22 and S23 in the Supporting Information for comparison with the experimental INS spectra of the three compounds. It is noted that, unlike (optical) far-IR and Raman spectroscopies, there are no symmetry-based INS selection rules. Thus, all phonon modes are active. Overall, there is a good match between experimental (by VISION at 5 K) and calculated INS in the region above 150 cm^{-1}. However, low-energy modes are difficult to calculate accurately. It should be pointed out that the current calculations do not account for any peaks of magnetic origin or spin-phonon coupling. In addition, the VASP[26a] and phonopy[26b] calculations, while giving phonons (and their symmetries and energies) and spin densities discussed below, are not able to address spin-phonon coupling in the solids. Spin-phonon couplings in other SMMs, in particular their roles in magnetic relaxation, have been the subjects of recent computations or modeling studies.[12,26]

Far-IR and Raman spectra of the three complexes recorded at 0 T and 5 K, revealing IR- (*u* symmetry) and Raman-active (*g* symmetry) phonons, are given in the Supporting Information (**Co-Cl**: Figure S24; **Co-Br**: Figure S25; **Co-I**: Figure S26). Since spin-phonon couplings, discussed below, involve some of the IR-active phonons and were observed in FIRMS, animations of the A_u and B_u phonons near the peaks of the magnetic transition around 20–75 cm^{-1} (14, 16, and 31 movies for **Co-Cl**, **Co-Br** and **Co-I**, respectively) have been made based on the VASP and phonopy calculations and are provided in Supporting Information. These animations show atomic displacements with contributions from both external and internal modes.

Studies of spin-phonon couplings in FIRMS spectra: Multiple phonons were found to be involved in spin-phonon couplings with the magnetic transition in FIRMS spectra of **Co-Cl** (Figures 7 and S1), leading to avoided crossings (also known as non-crossings or anticrossings). An avoided crossing is, in essence, the result of interactions between two states/levels of the same symmetries, leading to two new states/levels from mixing of the two original states/levels, as shown in Figure 7-Left.[43] When 1*s* orbitals from two H atoms interact to form σ bonding and σ* antibonding orbitals, it is essentially an avoided crossing of two 1*s* orbitals. Spin-phonon coupling here reflects how a vibration (with periodic motion of the atoms in a molecule) affects the magnetic levels in Figure 1. Recently, a vibronic model was used to account for similar couplings of vibrations in $Co(acac)_2(H_2O)_2$ ($S = 3/2$) with the $m_S = \pm 1/2, \pm 3/2$ levels.[13b]

In the FIRMS spectra of **Co-Cl** (Figures 7-Right and S1-Bottom), when a magnetic (spin) peak (**A**) is close to a phonon peak (**B**) with the same symmetry (i.e., both excitations belong to the same irreducible representation in the C_{2h} point group), the two couple, causing the peak of magnetic transition to take on the characteristic of the phonon peak and vice-versa. That is, the two coupled peaks carry both magnetic and phonon features.[13b] The avoided crossings are observed as peak **A** is blue-shifted by the increasing magnetic field. In Figure 7-Right and more clearly in Figure S1-Bottom (Supporting Information) without the white lines, peak **B** progressively picks up more magnetic features as the magnetic field increases, until it becomes the peak of the magnetic transition undergoing a blue-shift itself, while peak **A** turns into a phonon peak. Peak **B** continues the blue-shift until encountering another phonon (**C**) with the same symmetry. At this point, **B** and **C** undergo a new spin-phonon coupling, resulting in another avoided crossing. This process is repeated with two additional phonon peaks **D** and **E**. It should be pointed out that there might be spin-phonon couplings involving additional phonons. However, if they exist, they are not easily identified in Figure 7-Right. The observations of the spin-phonon couplings between magnetic transitions and IR-active *u*-symmetry phonons here are in contrast with the spin-phonon couplings in $Co(acac)_2(H_2O)_2$ and its isotopologues,[13b] in which the couplings were observed with Raman-active *g* phonons.

For the 2-D FIRMS map in Figure 7-Right, a simplified Hamiltonian for the coupling between the magnetic excited level $|\phi_j\rangle$ and *one* phonon excited state $|n\rangle$ is given by the following 2×2 matrix in Eq. 2:[13b]

$$H = \begin{pmatrix} E_{sp} & \Lambda \\ \Lambda & E_{ph} \end{pmatrix} \quad (2)$$

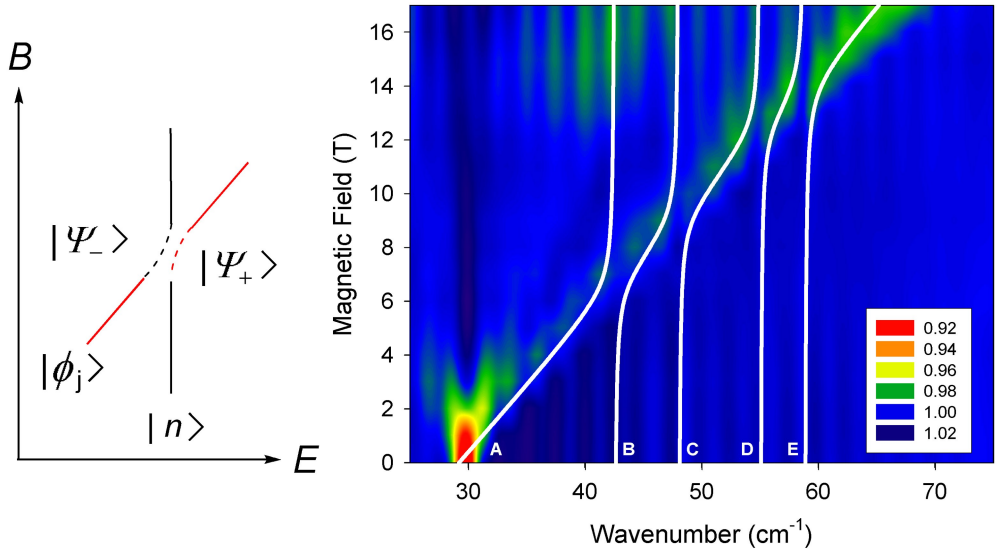

Figure 7. (Left) Schematic representation of an avoided crossing. Some of us have recently provided more detailed schematic views of the spin-phonon couplings in a Co(II) complex with axial anisotropy ($D<0$).[17d] (Right) FIRMS plot of **Co-Cl** spectra normalized by average, which minimizes phonon features that do not change with magnetic fields. The color trend from red to blue corresponds to absorption decrease. The white lines show the results of the spin-phonon coupling model using a 5×5 matrix in Eq. 4 below. Figure 7-Right is also shown in Figure S1-Bottom in the Supporting Information without the white lines to more clearly reveal the avoided crossings. The blue shifting transition is from the lowest magnetic level to the highest magnetic level of the ground spin quartet and corresponds to a specific direction of the external field with respect to the spin coordinate system (i.e., a turning point). These levels are not well-defined by m_s quantum numbers due to the mixing.[5]

in which E_{sp} and E_{ph} = Expected energies of the magnetic and phonon excitations, respectively; Λ = spin-phonon coupling constant.

Solving the matrix gives two eigenvalues $E_{\pm}$ (with the associated avoided-crossing peaks $|\Psi_{\pm}\rangle$) in the secular Eq. 3.

$$\begin{vmatrix} E_{sp}-E_{\pm} & \Lambda \\ \Lambda & E_{ph}-E_{\pm} \end{vmatrix} = 0 \qquad (3)$$

During the spin-phonon coupling, $|\Psi_{+}$ shifts to higher E_{+}, while $|\Psi_{-}$ shifts to lower E_{-} in the avoided crossing, as shown in Figure 7-Left. Eqs. 2–3 give a model to understand spin-phonon coupling in the FIRMS map and calculate the coupling constants Λ.

This model can be expanded to a 5×5 matrix in Eq. 4 involving the couplings of the magnetic transition with all four phonons **B**, **C**, **D** and **E** simultaneously. Eq. 4 ignores interactions (couplings) among phonons, as the off-diagonal elements between any two phonons are set to be 0. The ZFS peak (E_{sp}) was modeled every 0.5 T from 0 T to 17 T for the transmittance peak, giving the coupling constants Λ_1-Λ_4 of 1.3(1)–1.4(3) cm^{-1} in Table 2. If the spectra are instead fit using multiple 2×2 matrices in Eq. 2, the coupling constants are not appreciably different. It should be pointed out that **B**, **C**, **D**, and **E** are those phonons in the crystalline solid of **Co-Cl** that are observed to undergo spin-phonon couplings, even though there are additional IR-active phonons in the 30–80 cm^{-1} region, as listed in Table S1.

$$H = \begin{pmatrix} E_{sp} & \Lambda_1 & \Lambda_2 & \Lambda_3 & \Lambda_4 \\ \Lambda_1 & E_{ph1} & 0 & 0 & 0 \\ \Lambda_2 & 0 & E_{ph2} & 0 & 0 \\ \Lambda_3 & 0 & 0 & E_{ph3} & 0 \\ \Lambda_4 & 0 & 0 & 0 & E_{ph4} \end{pmatrix} \qquad (4)$$

Spin-phonon couplings are also observed in FIRMS maps of **Co-Br** (Figure 8-Left) and **Co-I** (Figure 8-Right) and also in Figures S2-Bottom and Figure S3-Bottom, respectively, without the white lines of spin-phonon couplings. Six phonons in **Co-Br** are noticed to couple with the magnetic transition, giving rise to avoided crossings as the latter blue-shifts due to the Zeeman effect (IR-active, *u*-symmetry phonons **B-G** in the 30–80 cm^{-1} region, Table S2). Simulations using a 7×7 matrix (Eq. S2 in Supporting Information) give the coupling constants of 1.0(3)-1.8(4) cm^{-1} in Table 2. For a crystalline solid of **Co-I**, nine phonons (**B-J** in Figure 8-Right) are shown to couple to the magnetic transition leading to several avoided crossings, as peak **A** moves to higher energy with increasing external magnetic field. Simulations using a 10×10 matrix (Eq. S3 in Supporting Information) give the coupling constants of 0.9(3)–2.0(4) cm^{-1} in Table 2.

Calculated spin densities of atoms in Co-X complexes

The DFT calculations using VASP also give spin densities, ρ_s, in **Co-X**, as summarized in Table 3 with detailed lists for each atom in Tables S13, S14 in Supporting Information. Although the

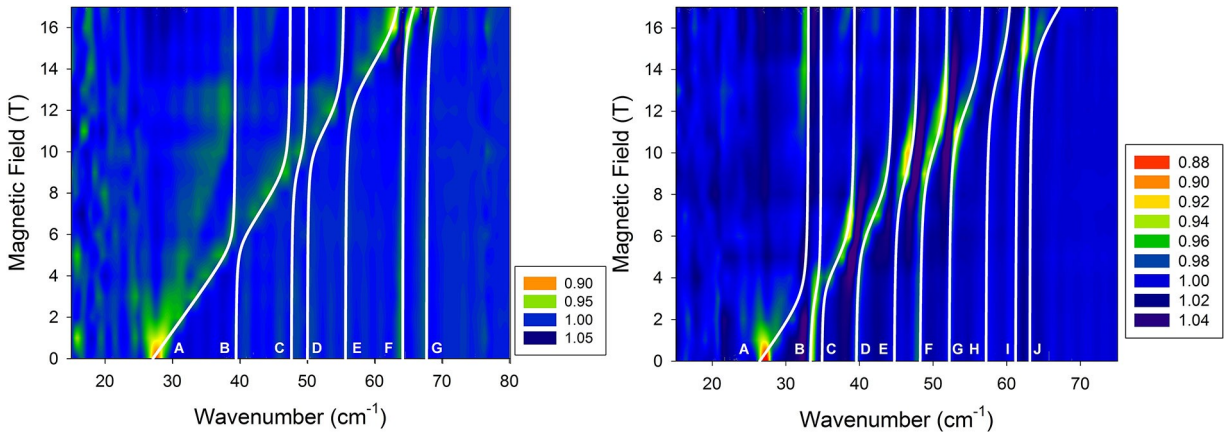

Figure 8. FIRMS plots of far-IR spectra normalized by average, which minimize phonon features that do not change with magnetic field: (Left) **Co-Br**; (Right) **Co-I**, revealing simulations of spin-phonon couplings. The color trend from red to blue corresponds to a decrease of absorption. The white lines show the results of the spin-phonon coupling model using a 7×7 matrix for **Co-Br** and a 10×10 matrix for **Co-I**, which are similar to those of the 5×5 matrix in Eq. 4 and are given in Supporting Information. Figure 8-Left (**Co-Br**) and -Right (**Co-I**) are also given in Figures S2-Bottom and S3-Bottom, respectively, without the white simulation lines here to more clearly show the avoided crossings.

Table 3. Calculated spin densities ρ_s of atoms in **Co-X**.

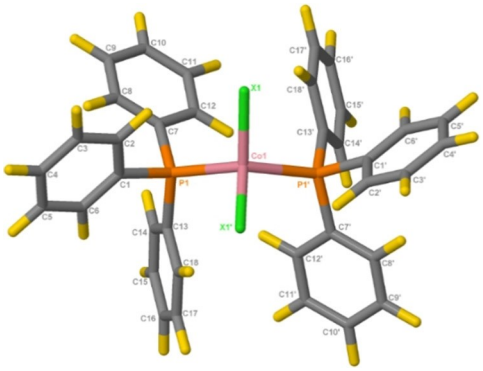

Atom	**Co-Cl**	**Co-Br**	**Co-I**
Co	2.585	2.570	2.553
X	6.69×10^{-2} (**Cl**)	6.85×10^{-2} (**Br**)	6.01×10^{-2} to 6.39×10^{-2} (**I**)
P	2.06×10^{-2}	1.92×10^{-2}	1.55×10^{-2} to 1.94×10^{-2}
C	-2.02×10^{-4} to -6.38×10^{-4} 1.21×10^{-4} to 2.98×10^{-3}	-1.50×10^{-4} to -5.36×10^{-4} 3.90×10^{-4} to 2.93×10^{-3}	-6.62×10^{-6} to -1.04×10^{-3} 4.40×10^{-8} to 5.07×10^{-3}
H	-1.77×10^{-5} to -5.65×10^{-5} 2.40×10^{-7} to 8.40×10^{-5}	-1.89×10^{-5} to -4.92×10^{-5} 1.21×10^{-6} to 9.47×10^{-5}	-2.70×10^{-6} to -4.10×10^{-5} 5.85×10^{-6} to 8.85×10^{-5}
Total	2.797	2.783	2.747

The structure of **Co-Cl** and its atom labelling are given here as an example. Details of the spin densities of **Co-X** are given in Tables S13 and S14 in the Supporting Information.

VASP calculations here are not of high-level, they provide a quantitative scale, revealing how the spin is dispersed onto X, P, C and peripheral H atoms in the molecules.[1r] VASP partitions electrons according to the Wigner-Seitz radius a_e in Eq. 5:[44]

$$a_e = (3/4\pi n_e)^{1/3} \quad (5)$$

where n_e is the particle density of electrons; a_e is the radius "occupied" by one atom in a sample, and each atom is considered as a sphere.

This method does not include spin densities in bonds between atoms. Therefore, the total spin densities (sums of those on all atoms) of 2.80, 2.78 and 2.75 for **Co-Cl**, **Co-Br** and **Co-I**, respectively, are smaller than 3 (=3 unpaired electrons) on

the molecules. The results in Table 3 show that the unpaired electron densities are transferred from the central Co(II) ions to ligand atoms, although the metal ions retain 2.59, 2.57 and 2.55 unpaired electrons (>92% of total spin in each of the three compounds, not counting the spin densities between bonds), respectively. That the spin density is mostly on the Co(II) ion in **Co-X** is consistent with the above simple LFT that describes the complexes as pure d^7 systems, i.e., as having nearly "innocent" ligands. This is in contrast to the case of a diiodide complex of Mn(III) (d^4, $S=2$) wherein a valence tautomer that can be described as Mn(II) $[MnI^{\bullet}]^{2+}$, as opposed to the innocent Mn(III) $[MnI^{-}]^{2+}$, leads to unusual ZFS.[45] Among ligand atoms, the halides X carry very small, yet the highest spin densities (6.01×10^{-2} to 6.85×10^{-2}), followed by the P atoms (1.55×10^{-2} to 2.06×10^{-2}). These densities are positive, as those of some C and H atoms of the phenyl groups in the PPh_3 ligands (Tables S13 and S14), indicating that spins on the α atoms in the molecules are parallel to those on the Co(II) ion. Other C and H atoms, however, have negative spin densities, i.e., the spin densities on these atoms have opposite polarization to that on the Co(II) ion, X, and P atoms.

Our results are consistent with NMR studies of paramagnetic compounds,[46] which show that ligand resonances are typically shifted by electron spin densities on the ligand atoms.[46] The signs of ρ_s in Table 3 indicate that both spin delocalization and polarization mechanisms, which are used as a model to explain spin delocalization in paramagnetic molecules,[46a,b] likely account for the transfer of spin densities in **Co-X**.

It is interesting to note that the slight decrease of spin density on the Co(II) ion from **Co-Cl** (2.585), **Co-Br** (2.570), to **Co-I** (2.553) parallels the drop of D' from 14.89(2), to 13.83(2), and to 13.63(10) cm^{-1} (HFEPR results) for the three complexes, as shown in Figure S29 in Supporting Information. For $Co(acac)_2(H_2O)_2$, also a SMM,[1r,13b, c] but with only light atom (Period 2) donor ligands, the calculated spin density of 2.81 (by the same VASP program) on its Co(II) ion and D' of 57 cm^{-1} are both larger than those of **Co-X**. At least among these four Co(II) complexes, the larger spin density on a metal ion, the larger ZFS in the complex. It should be pointed out that the number of complexes here [four including $Co(acac)_2(H_2O)_2$] is limited, and different DFT programs may give different calculated spin densities. Studies of more compounds are needed to see if there is a correlation between the spin densities and magnetitudes of ZFS. In addition, the current VASP calculations are not able to address spin-phonon coupling,[12] as indicated earlier. Thus, additional studies are needed to understand how the spin density affects ZFS in a complex and how the lattice and molecular motions (i.e., phonons) that are coupled to the magnetic excited levels impact the spin density.

Conclusion

The current work demonstrates that magneto far-IR spectroscopy is a powerful technique for probing spin-phonon coupling in SMMs, giving the intensity of these interactions and determining energies of magnetic excited levels in the complexes. INS spectroscopy is a unique, zero-field technique to identify both magnetic transitions and all phonons in the molecules, providing insight as to the phonons involved in these couplings, when combined with DFT phonon and INS calculations. Herein, for **Co-X** with centrosymmetric C_{2h} crystallographic symmetry, INS spectra showing all phonons, in combination with far-IR and Raman spectra showing *u*- and *g*-symmetry phonons, respectively, give a comprehensive characterization of phonons in the region of interest. The current determination of complete spin Hamiltonian parameters of **Co-X** by a combination of spectroscopies provides a rare view of the magnetic separations in these complexes from different spectroscopic perspectives and makes an excellent opportunity to compare the techniques. Field- and frequency-domain resonance methods give entirely consistent results, whereas magnetometry is less reliable. As was pointed out by Pavlov *et al.*, a combination of experimental techniques is optimal to determine ZFS in SMMs, such as those of Co(II).[47] LFT work accurately calculated the *D*, *E* parameters and pointed to the origin of the ZFS for the three complexes. The current studies of the spin-phonon coupling will help understand magnetic relaxation in SMMs and molecular qubits and develop guidance to reduce or avoid the couplings.

It should be pointed out that the current work experimentally determines the magnetic excited levels and degrees of their couplings with nearby phonons (as coupling constants). Additional studies, especially those with computations or modelings as recently reported for other compounds,[12] are needed to provide an insight into the spin-phonon coupling. Such investigations are expected to correlate the magnetic and phonon properties of the compounds, including why only *u*-symmetry phonons in **Co-X** are involved in spin-phonon coupling, how the coupling phonons impact the ZFS parameters and the spin densities, and how the intensity of this coupling affects other interactions such as crystal field, ZFS, and Zeeman splitting.

Experimental

Compounds **Co-Cl**, **Co-Br**, and **Co-I** were prepared by literature methods.[4a–c] Powder X-ray diffraction of typical **Co-Cl**, **Co-Br** and **Co-I** samples in the studies are given in Figure S28.

Variable-field INS data were collected at the Disc Chopper Spectrometer (DCS) at the NIST Center for Neutron Research (NCNR). A powder sample of **Co-Cl** (2 g) was measured in the 1.5–1.6 K range at 0 T with $E_i=73$ cm^{-1}, and at 10 T with $E_i=54$ cm^{-1}, in order to compare the results of VT and variable-field INS. All data were processed on DAVE.[48] VT INS spectra were collected on the Vibrational Spectrometer (VISION) at the Spallation Neutron Source (SNS), ORNL. For each measurement, approximately 0.2 g of the powder sample was sealed in an aluminum can. The aluminum can was then fixed on the end of the sample holder and placed inside the neutron beam. VISION has two detector banks, forward- and back-scattering, providing data for low and high $|\boldsymbol{Q}|$ scattering, respectively.[22e] As an indirect-geometry INS spectrometer,[22e] data of low scattering angles, including magnetic scattering, are more intense in the forward-scattering detectors at VISION.

The far-IR setups with applied magnetic fields at the National High Magnetic Field Laboratory (NHMFL, Tallahassee, Florida, USA; FIRMS) and at the electron storage ring BESSY II (Berlin, Germany; FD-FT THz-EPR) have been used. The two groups practicing it in the current work, however, use different magnet configurations (vertical-bore or split-coil) and process the data differently. FIRMS spectra were collected at NHMFL using a Bruker Vertex 80v Fourier-transform infrared (FT-IR) spectrometer coupled with a 17.5 T vertical-bore superconducting magnet. The experimental setup is equipped with a mercury lamp and a composite silicon bolometer (Infrared Laboratories), as an incoherent (sub)-THz radiation source and detector, respectively. The THz radiation propagates in free-space inside the optical beamline, connecting the output of the spectrometer and top of the sample probe. The radiation then passes through the brass lightpipe over a distance of 2.5 m from room temperature to the field center. The probe and beamline are evacuated to eliminate strong parasitic absorptions of the air. The samples are mulls of *n*-eicosane and powder (~2 mg) of each complex. Both the sample and the bolometer were cooled by low-pressure helium gas to ~5 K. The spectrum of the THz radiation transmitted through the samples was measured between 10 and 720 cm^{-1} (0.3–21.6 THz) with a resolution of 0.3 cm^{-1} (9 GHz), acquisition time of 3 min, and 5 kHz scanner speed.

FD-FT THz-EPR experiments were performed at the THz beamline of the BESSY II storage ring and employed a 10 T split-coil superconducting magnet (Oxford-Spectromag 4000) equipped with wedged *z*-cut quartz windows in transmission geometry. The temperature was varied between 2 K and 300 K and the field from 0 to 7 T. To vary the temperature, we either used an Oxford-Optistat cryostat with quartz windows in transmission geometry or, for magnetic measurements, a VT insert in the magnet. The FT-IR spectrometer was a Bruker IFS125 HR with its internal Hg-source (Q202) and set to 0.5 cm^{-1} resolution (0.2 cm^{-1} for absorbance measurements in the SI), 40 kHz scanner frequency, 100 sweeps and an IR-Labs 4.2 K/Si-bolometer (and a 1.6 K one for temperature-dependent measurements shown in SI). The acquisition time for a single raw spectrum was 3 min and transmittance data presented in Figures S8 and S11 in the Supporting Information were measured in 10 min.

Errors in $2D'$ values were obtained as described below: (1) For INS spectra, they were estimated to be 10% of the full width at half maximum (FWHM) of the peaks of magnetic transitons in baseline-corrected spectra (0 T) in the 20–40 cm^{-1} range. (2) For FIRMS and HFEPR spectra, the errors were obtained from simulations of the spectra. (3) For FD-FT THz-EPR spectra, they were obtained from visual inspection of the agreement between experimental and simulated spectra.

HFEPR was performed using the EMR facility at NHMFL. The facility operates a transmission spectrometer described elsewhere,[49] which was modified by the use of Virginia Diodes Inc. (VDI, Charlottesville, VA, USA) sources, generating sub-THz radiation in the 50–640 GHz frequency range. In some experiments requiring higher frequencies (>700 GHz), backward-wave oscillators were used as sources of sub-THz radiation. The spectrometer is associated with a 15/17 T warm-bore superconducting magnet. The samples were measured both "as is" which allowed them to orient (torque) in the magnetic field, or as pellets mixed with *n*-eicosane. About 30–60 mg of the powder samples were used in each measurement. HFEPR spectra were typically collected at 5–10 K.

Experimental details of the Raman spectroscopic studies and results are given in Supporting Information.

In the calculations of phonons for **Co-Cl**, **Co-Br**, and **Co-I**, geometry optimizations were performed on the single-crystal X-ray structures of the compounds (Table S5).[4a,b,e] The optimized structure at 0 T was used for the phonon calculations. Spin-polarized, periodic DFT calculations were performed using VASP to generate the force constants on the supercell (284 atoms) created by phonopy.[26b] Phonopy was further used to produce phonon frequencies and polarization vectors (also gives irreducible representations). Then, OCLIMAX[50] calculates INS spectra using VISION parameters (and generating 0 K spectra). Jmol was used to create the phonon movies shown in Supporting Information.

The unpaired electron spin density was calculated using VASP on the optimized structure. Spin-polarized, periodic DFT calculations were performed using VASP with the Projector Augmented Wave (PAW)[51] method and the local density approximation (GGA)[52] + U (U = 4.4 eV)[51a,53] exchange correlation functional. The energy cut off was 800 eV for the plane-wave basis of the valence electrons. The total energy tolerance for electronic structure minimization was 10^{-8} eV. The optB86b-vdW, a non-local correlation functional that approximately accounts for dispersion interactions, was applied.[54] For the structure relaxation, a 1×2×1 Monkhorst-Pack mesh was used. Wigner-Seitz radii (Å): H = 0.370; C = 0.863; P = 1.233, Cl = 1.111, Br = 1.164, I = 1.487, Co = 1.302.

Acknowledgments

US National Science Foundation (NSF, CHE-1900296 to Z.-L.X. and DMR-2004732 to S.H.) and a Shull Wollan Center Graduate Research Fellowship (Z.L.) are acknowledged for partial support of the research. Part of this work was performed at the National High Magnetic Field Laboratory which is supported by NSF Cooperative Agreement No. DMR-1644779 and the State of Florida. We acknowledge the support of the National Institute of Standards and Technology, U.S. Department of Commerce, in providing the Disk Chopper Spectrometer (DCS) used in this work and HZB, Germany, for the allocation of the FD-FT THz-EPR instrument time. Additional neutron scattering experiments were conducted at the VISION beamline at ORNL's Spallation Neutron Source, which is supported by the Scientific User Facilities Division, Office of Basic Energy Sciences (BES), U.S. Department of Energy (DOE), under Contract No. DE-AC0500OR22725 with UT Battelle, LLC. The computing resources were made available through the VirtuES and the ICEMAN projects, funded by the Laboratory Directed Research and Development program and the Compute and Data Environment for Science (CADES) facility at ORNL. We thank Dr. Wei Zhou of the NIST Center for Neutron Research (NCNR) for help with the DCS experiment on **Co-Cl**, Dr. Thomas Lohmiller (HZB) for help with simulation of the FD-FT THz-EPR data, Dr. Andrew Ozarowski (NHMFL) for his EPR simulation and fit program SPIN, Prof. Jesper Bendix, Copenhagen University, Denmark, for the program Ligfield, and Prof. Michael A. Hitchman, University of Tasmania, Australia, for helpful discussions at the time of the original HFEPR study on **Co-Cl**, which are now relevant.

Conflict of Interest

The authors declare no conflict of interest.

Keywords: avoided crossings · magnetic relaxation · single-molecule magnets (SMMs) · spin-phonon coupling · zero-field splitting (ZFS)

[1] a) C. Benelli, D. Gatteschi, *Introduction to Molecular Magnetism: From Transition Metals to Lanthanides*, Wiley-VCH, Weinheim, **2015**; b) J. M. Frost, K. L. M. Harriman, M. Murugesu, *Chem. Sci.* **2016**, *7*, 2470–2491; c) R. A. Layfield, *Organometallics* **2014**, *33*, 1084–1099; d) J. Krzystek, J. Telser, *Dalton Trans.* **2016**, *45*, 16751–16763; e) E. J. L. McInnes, R. E. P. Winpenny, *Molecular Magnets in Comprehensive Inorganic Chemistry II* (Ed.: K. Poeppelmeier), Elsevier, Amsterdam, **2013**, pp. 371–395; f) F. Neese, D. A. Pantazis, *Faraday Discuss.* **2011**, *148*, 229–238; g) S. Gao, Ed., *Molecular Nanomagnets and Related Phenomena*, Springer, Berlin, **2015**; h) P. Zhang, L. Zhang, J. Tang, *Dalton Trans.* **2015**, *44*, 3923–3929; i) J.-L. Liu, Y.-C. Chen, M.-L. Tong, *Chem. Soc. Rev.* **2018**, *47*, 2431–2453; j) G. A. Craig, M. Murrie, *Chem. Soc. Rev.* **2015**, *44*, 2135–2147; k) J. D. Rinehart, J. R. Long, *Chem. Sci.* **2011**, *2*, 2078–2085; l) D. Gatteschi, R. Sessoli, *Angew. Chem. Int. Ed.* **2003**, *42*, 268–297; *Angew. Chem.* **2003**, *115*, 278–309; m) S. Demir, I.-R. Jeon, J. R. Long, T. D. Harris, *Coord. Chem. Rev.* **2015**, *289*, 149–176; n) R. Boča, *Coord. Chem. Rev.* **2004**, *248*, 757–815; o) M. Shatruk, S. Gómez-Coca, K. R. Dunbar, *Molecular Magnetism, in Molecular Magnetic Materials: Concepts and Applications* (Eds.: B. Sieklucka, D. Pinkowicz), Wiley-VCH, Weinheim, **2017**, pp. 29–77; p) M. Yamashita, K. Katoh, *Single Molecule Magnets, in Molecular Magnetic Materials: Concepts and Applications* (Eds.: B. Sieklucka, D. Pinkowicz), Wiley-VCH, Weinheim, **2017**, pp. 79–101; q) D. Gatteschi, R. Sessoli, J. Villain, *Molecular Nanomagnets*, Oxford University Press, Oxford, UK, **2006**; r) S. E. Stavretis, E. Mamontov, D. H. Moseley, Y. Cheng, L. L. Daemen, A. J. Ramirez-Cuesta, Z.-L. Xue, *Phys. Chem. Chem. Phys.* **2018**, *20*, 21119–21126.

[2] a) L. Chen, J. Zhou, H.-H. Cui, A.-H. Yuan, Z. Wang, Y.-Q. Zhang, Z.-W. Ouyang, Y. Song, *Dalton Trans.* **2018**, *47*, 2506–2510; b) T. T. da Cunha, V. M. M. Barbosa, W. X. C. Oliveira, E. F. Pedroso, D. M. A. García, W. C. Nunes, C. L. M. Pereira, *Inorg. Chem.* **2020**, *59*, 12983–12987.

[3] M. Dey, N. Gogoi, *Angew. Chem. Int. Ed.* **2013**, *52*, 12780–12782; *Angew. Chem.* **2013**, *125*, 13014–13016.

[4] a) M. R. Saber, K. R. Dunbar, *Chem. Commun.* **2014**, *50*, 12266; b) F. Yang, Q. Zhou, Y.-Q. Zhang, G. Zeng, G. Li, Z. Shi, B. Wang, S. Feng, *Chem. Commun.* **2013**, *49*, 5289; c) R. Boča, J. Miklovič, J. Titiš, *Inorg. Chem.* **2014**, *53*, 2367–2369; d) J. Krzystek, S. A. Zvyagin, A. Ozarowski, A. T. Fiedler, T. C. Brunold, J. Telser, *J. Am. Chem. Soc.* **2004**, *126*, 2148; e) R. L. Carlin, R. D. Chirico, E. Sinn, G. Mennenga, L. J. De Jongh, *Inorg. Chem.* **1982**, *21*, 2218–2222; f) J. Lu, I. O. Ozel, C. A. Belvin, X. Li, G. Skorupskii, L. Sun, B. K. Ofori-Okai, M. Dincă, N. Gedik, K. A. Nelson, *Chem. Sci.* **2017**, *8*, 7312–7323; g) M. Sundararajan, D. Ganyushin, S. Ye, F. Neese, *Dalton Trans.* **2009**, 6021–6036.

[5] a) J. R. Pilbrow, *J. Magn. Reson.* **1978**, *31*, 479–490; b) P. Gast, E. J. J. Groenen, *EPR Interactions – g-Anisotropy, in eMagRes*, **2016**, pp. 1435–1444.

[6] a) F. E. Mabbs, D. J. Machin, *Magnetism and Transition Metal Complexes*, Dover Publications, Inc., Mineola, New York, **1973**; b) F. Neese, *J. Chem. Phys.* **2007**, *127*, 164112; c) W. D. Horrocks, D. A. Burlone, *J. Am. Chem. Soc.* **1976**, *98*, 6512–6516; d) J. A. Larrabee, C. M. Alessi, E. T. Asiedu, J. O. Cook, K. R. Hoerning, L. J. Klingler, G. S. Okin, S. G. Santee, T. L. Volkert, *J. Am. Chem. Soc.* **1997**, *119*, 4182–4196.

[7] a) L. Banci, A. Bencini, C. Benelli, D. Gatteschi, C. Zanchini, in *Structures versus Special Properties, Vol. 52*, Springer, Berlin, Heidelberg, **1982**, pp. 37–86; b) D. M. Duggan, D. N. Hendrickson, *Inorg. Chem.* **1975**, *14*, 1944–1956; c) L. C. Kuo, M. W. Makinen, *J. Am. Chem. Soc.* **1985**, *107*, 5255–5261; d) M. W. Makinen, L. C. Kuo, M. B. Yim, G. B. Wells, J. M. Fukuyama, J. E. Kim, *J. Am. Chem. Soc.* **1985**, *107*, 5245–5255; e) M. W. Makinen, M. B. Yim, *Proc. Natl. Acad. Sci. USA* **1981**, *78*, 6221–6225; f) A. C. Rizzi, C. D. Brondino, R. Calvo, R. Baggio, M. T. Garland, R. E. Rapp, *Inorg. Chem.* **2003**, *42*, 4409–4416.

[8] a) J. Krzystek, S. A. Zvyagin, A. Ozarowski, S. Trofimenko, J. Telser, *J. Magn. Reson.* **2006**, *178*, 174–183; b) J. Krzystek, J.-H. Park, M. W. Meisel, M. A. Hitchman, H. Stratemeier, L.-C. Brunel, J. Telser, *Inorg. Chem.* **2002**, *41*, 4478–4487; c) R. Ruamps, R. Maurice, L. Batchelor, M. Boggio-Pasqua, R. Guillot, A. L. Barra, J. Liu, E.-E. Bendeif, S. Pillet, S. Hill, T. Mallah, N. Guihéry, *J. Am. Chem. Soc.* **2013**, *135*, 3017–3026; d) P. Tin, S. E. Stavretis, M. Ozerov, J. Krzystek, A. N. Ponomaryov, S. A. Zvyagin, J. Wosnitza, C.-C. Chen, P. P. Y. Chen, J. Telser, Z.-L. Xue, *Appl. Magn. Reson.* **2020**, *51*, 1411–1432; e) J. Lawrence, C. C. Beedle, E.-C. Yang, J. Ma, S. Hill, D. N. Hendrickson, *Polyhedron* **2007**, *26*, 2299–2303.

[9] R. P. v. Stapele, H. G. Beljers, P. F. Bongers, H. Zijlstra, *J. Chem. Phys.* **1966**, *44*, 3719–3725.

[10] J. Titiš, J. Miklovič, R. Boča, *Inorg. Chem. Commun.* **2013**, *35*, 72–75.

[11] a) M. J. Graham, J. M. Zadrozny, M. S. Fataftah, D. E. Freedman, *Chem. Mater.* **2017**, *29*, 1885–1897; b) E. Moreno-Pineda, C. Godfrin, F. Balestro, W. Wernsdorfer, M. Ruben, *Chem. Soc. Rev.* **2018**, *47*, 501–513; c) R. Orbach, H. J. Stapleton, *Electron spin-lattice relaxation, in Electron Paramagnetic Resonance* (Ed.: S. Geschwind), Plenum Press, New York, **1972**, pp. 121–216.

[12] a) D. Aravena, E. Ruiz, *Dalton Trans.* **2020**, *49*, 9916–9928; b) A. Lunghi, F. Totti, R. Sessoli, S. Sanvito, *Nat. Commun.* **2017**, *8*, 14620; c) L. Escalera-Moreno, N. Suaud, A. Gaita-Ariño, E. Coronado, *J. Phys. Chem. Lett.* **2017**, *8*, 1695–1700; d) R. Mirzoyan, R. G. Hadt, *Phys. Chem. Chem. Phys.* **2020**, *22*, 11249–11265; e) G. Czap, P. J. Wagner, J. Li, F. Xue, J. Yao, R. Wu, W. Ho, *Phys. Rev. Lett.* **2019**, *123*, 106803.

[13] a) Y. Rechkemmer, F. D. Breitgoff, M. van der Meer, M. Atanasov, M. Hakl, M. Orlita, P. Neugebauer, F. Neese, B. Sarkar, J. van Slageren, *Nat. Commun.* **2016**, *7*, 10467; b) D. H. Moseley, S. E. Stavretis, K. Thirunavukkuarasu, M. Ozerov, Y. Cheng, L. L. Daemen, J. Ludwig, Z. Lu, D. Smirnov, C. M. Brown, A. Pandey, A. J. Ramirez-Cuesta, A. C. Lamb, M. Atanasov, E. Bill, F. Neese, Z.-L. Xue, *Nat. Commun.* **2018**, *9*, 2572; c) S. E. Stavretis, Y. Cheng, L. L. Daemen, C. M. Brown, D. H. Moseley, E. Bill, M. Atanasov, A. J. Ramirez-Cuesta, F. Neese, Z.-L. Xue, *Eur. J. Inorg. Chem.* **2019**, *2019*, 1119–1127; d) D. H. Moseley, S. E. Stavretis, Z. Zhu, M. Guo, C. M. Brown, M. Ozerov, Y. Cheng, L. L. Daemen, R. Richardson, G. Knight, K. Thirunavukkuarasu, A. J. Ramirez-Cuesta, J. Tang, Z.-L. Xue, *Inorg. Chem.* **2020**, *59*, 5218–5230.

[14] a) M. Schwoerer, H. C. Wolf, *Molecular and Lattice Dynamics in Organic Molecular Crystals in Organic Molecular Solids*, Wiley-VCH, Weinheim, **2007**, pp. 89–124; b) P. M. A. Sherwood, *Vibrational Spectroscopy of Solids*, Cambridge University Press, Cambridge, UK, **1972**, pp. 22–25.

[15] a) C. Kittel, Introduction to Solid State Physics, 8 ed., **2004**, pp. 89–130; b) M. T. Dove, Introduction to Lattice Dynamics, Vol. Cambridge Topics in Mineral Physics and Chemistry, Cambridge University Press, **1993**.

[16] a) G. C. Brackett, P. L. Richards, W. S. Caughey, *J. Chem. Phys.* **1971**, *54*, 4383–4401; b) G. C. Brackett, Ph.D. dissertation, University of California, Berkeley **1970**.

[17] a) Y. Rechkemmer, J. E. Fischer, R. Marx, M. Dörfel, P. Neugebauer, S. Horvath, M. Gysler, T. Brock-Nannestad, W. Frey, M. F. Reid, J. van Slageren, *J. Am. Chem. Soc.* **2015**, *137*, 13114–13120; b) R. Marx, F. Moro, M. Dorfel, L. Ungur, M. Waters, S. D. Jiang, M. Orlita, J. Taylor, W. Frey, L. F. Chibotaru, J. van Slageren, *Chem. Sci.* **2014**, *5*, 3287–3293; c) K. Ray, A. Begum, T. Weyhermüller, S. Piligkos, J. van Slageren, F. Neese, K. Wieghardt, *J. Am. Chem. Soc.* **2005**, *127*, 4403–4415; d) S. E. Stavretis, D. H. Moseley, F. Fei, H.-H. Cui, Y. Cheng, A. A. Podlesnyak, X. Wang, L. L. Daemen, C. M. Hoffmann, M. Ozerov, Z. Lu, K. Thirunavukkuarasu, D. Smirnov, T. Chang, Y.-S. Chen, A. J. Ramirez-Cuesta, X.-T. Chen, Z.-L. Xue, *Chem. Eur. J.* **2019**, *25*, 15846–15857; e) A. Świtlicka, B. Machura, M. Penkala, A. Bieńko, D. C. Bieńko, J. Titiš, C. Rajnák, R. Boča, A. Ozarowski, M. Ozerov, *Inorg. Chem.* **2018**, *57*, 12740–12755; f) P. C. Bunting, M. Atanasov, E. Damgaard-Møller, M. Perfetti, I. Crassee, M. Orlita, J. Overgaard, J. van Slageren, F. Neese, J. R. Long, *Science* **2018**, *362*, eaat7319; g) S.-D. Jiang, D. Maganas, N. Levesanos, E. Ferentinos, S. Haas, K. Thirunavukkuarasu, J. Krzystek, M. Dressel, L. Bogani, F. Neese, P. Kyritsis, *J. Am. Chem. Soc.* **2015**, *137*, 12923–12928; h) J.-J. Liu, Y.-S. Meng, I. Hlavička, M. Orlita, S.-D. Jiang, B.-W. Wang, S. Gao, *Dalton Trans.* **2017**, *46*, 7408–7411; i) M. A. Hay, A. Sarkar, G. A. Craig, L. Bhaskaran, J. Nehrkorn, M. Ozerov, K. E. R. Marriott, C. Wilson, G. Rajaraman, S. Hill, M. Murrie, *Chem. Sci.* **2019**, *10*, 6354–6361; j) S. Haas, University of Stuttgart **2015**; k) J. Nehrkorn, K. Holldack, R. Bittl, A. Schnegg, *J. Magn. Reson.* **2017**, *280*, 10–19; l) A. Schnegg, J. Behrends, K. Lips, R. Bittl, K. Holldack, *Phys. Chem. Chem. Phys.* **2009**, *11*, 6820–6825; m) P. Kumar, D. J. SantaLucia, K. Kaniewska-Laskowska, S. V. Lindeman, A. Ozarowski, J. Krzystek, M. Ozerov, J. Telser, J. F. Berry, A. T. Fiedler, *Inorg. Chem.* **2020**, *59*, 16178–16193; n) C. N. Widener, A. N. Bone, M. Ozerov, R. Richardson, Z. Lu, K. Thirunavukkuarasu, D. Smirnov, X.-T. Chen, Z.-L. Xue, *Chin. J. Inorg. Chem.* **2020**, *35*, 1149–1156.

[18] E. Y. Misochko, A. V. Akimov, D. V. Korchagin, J. Nehrkorn, M. Ozerov, A. V. Palii, J. M. Clemente-Juan, S. M. Aldoshin, *Inorg. Chem.* **2019**, *58*, 16434–16444.

[19] V. P. Gnezdilov, V. V. Eremenko, A. V. Peschansky, V. I. Fomin, *Fiz. Nizk. Temp. (Low Temp. Phys.)* **1991**, *17*, 253–258.

[20] R. J. H. Clark, T. J. Dines, *Electronic Raman spectroscopy, in Advances in Infrared and Raman Spectroscopy, Vol. 9* (Eds.: R. J. H. Clark, R. E. Hester), Heyden & Son, London, **1982**, pp. 282–360.

[21] G. E. Bacon, *Neutron Scattering in Chemistry*, Butterworth, London, **1977**.

[22] a) A. Furrer, O. Waldmann, *Rev. Mod. Phys.* **2013**, *85*, 367–420; b) R. Basler, C. Boskovic, G. Chaboussant, H. U. Güdel, M. Murrie, S. T. Ochsenbein, A. Sieber, *ChemPhysChem* **2003**, *4*, 910–926; c) D. Gatteschi, *J. Phys. Chem. B* **2000**, *104*, 9780–9787; d) M. A. Dunstan, R. A. Mole, C. Boskovic, *Eur. J. Inorg. Chem.* **2019**, *2019*, 1090–1105; e) Z.-L. Xue, A. J. Ramirez-Cuesta, C. M. Brown, S. Calder, H. Cao, B. C. Chakoumakos, L. L. Daemen, A. Huq, A. I. Kolesnikov, E. Mamontov, A. A. Podlesnyak, X. Wang, *Eur. J. Inorg. Chem.* **2019**, 1065–1089; f) M. J. Giansiracusa, M. Vonci, W. Van den Heuvel, R. W. Gable, B. Moubaraki, K. S. Murray, D. Yu, R. A. Mole, A. Soncini, C. Boskovic, *Inorg. Chem.* **2016**, *55*, 5201–5214.

[23] B. S. Hudson, *Vib. Spectrosc.* **2006**, *42*, 25–32.

[24] a) S. C. Hunter, A. A. Podlesnyak, Z.-L. Xue, *Inorg. Chem.* **2014**, *53*, 1955–1961; b) S. E. A. M. Stavretis, A. A. Podlesnyak, S. C. Hunter, F. Neese, Z.-L. Xue, *Inorg. Chem.* **2015**, *54*, 9790–9801; c) L. Chen, H.-H. Cui, S. E. Stavretis, S. C. Hunter, Y.-Q. Zhang, X.-T. Chen, Y.-C. Sun, Z. Wang, Y. Song, A. A. Podlesnyak, Z.-W. Ouyang, Z.-L. Xue, *Inorg. Chem.* **2016**, *55*, 12603–12617.

[25] a) E. Colacio, J. Ruiz, E. Ruiz, E. Cremades, J. Krzystek, S. Carretta, J. Cano, T. Guidi, W. Wernsdorfer, E. K. Brechin, *Angew. Chem. Int. Ed.* **2013**, *52*, 9130–9134; *Angew. Chem.* **2013**, *125*, 9300–9304; b) A. N. Bone, S. E. Stavretis, J. Krzystek, Z. Liu, Q. Chen, Z. Gai, X. Wang, C. A. Steren, X. B. Powers, A. A. Podlesnyak, X.-T. Chen, J. Telser, H. Zhou, Z.-L. Xue, *Polyhedron* **2020**, *184*, 114488.

[26] a) The Vienna Ab initio Simulation Package: atomic scale materials modelling from first principles; b) A. Togo, VASP & Phonopy Calculation **2009**. https://phonopy.github.io/phonopy/vasp-dfpt.html

[27] C. Simo, S. Holt, *Inorg. Chem.* **1968**, *7*, 2655–2657.

[28] A. A. G. Tomlinson, C. Bellitto, O. Piovesana, C. Furlani, *J. Chem. Soc. Dalton Trans.* **1972**, 350–354.

[29] J. P. Jesson, S. Trofimenko, D. R. Eaton, *J. Am. Chem. Soc.* **1967**, *89*, 3148–3158.

[30] In Cs_3CoCl_5, the $[CoCl_4]^{2-}$ unit has D_{2d} symmetry, but is tetragonally elongated: Cl–Co-Cl angle = 106°. The labels used are appropriate for each of T_d, D_{2d}, and C_{2v} point group symmetry. Horrocks and Barlone use a different convention that leads to the ground state being $^4A_1$ in all three point group symmetries, but gives non-standard symmetry labels to the T_d and D_{2d} cases, which we find to be confusing, even if technically correct.

[31] J. E. Davies, M. Gerloch, D. J. Phillips, *J. Chem. Soc. Dalton Trans.* **1979**, 1836–1842.

[32] G. Miessler, P. J. Fischer, Donald A. Tarr, *Inorganic Chemistry*, 5 ed., Pearson, New York, **2013**, pp. 388.

[33] M. Brorson, C. E. Schaeffer, *Inorg. Chem.* **1988**, *27*, 2522–2530.

[34] J. Bendix, *2.55 - Ligfield, in Comprehensive Coordination Chemistry II* (Eds.: J. A. McCleverty, T. J. Meyer), Pergamon, Oxford, **2003**, pp. 673–676.

[35] a) P. W. M. Jacobs, *Group Theory with Applications in Chemical Physics*, Cambridge University Press, Cambridge, UK, **2005**; b) G. F. Koster, J. O. Dimmock, R. G. Wheeler, H. Statz, *Properties of The Thirty-Two Point Groups*, MIT Press, Cambridge, MA, **1963**.

[36] K. S. Pedersen, J. Dreiser, J. Nehrkorn, M. Gysler, M. Schau-Magnussen, A. Schnegg, K. Holldack, R. Bittl, S. Piligkos, H. Weihe, P. Tregenna-Piggott, O. Waldmann, J. Bendix, *Chem. Commun.* **2011**, *47*, 6918–6920.

[37] a) The intensity of the magnetic resonance absorption decreases and spreads out in high magnetic fields, because the intensity and frequency of the transitions are dependent on the direction of magnetic field with respect to the magnetic anisotropy *D*- and *g*-tensors in each microcrystallite of the powder sample. Though the microcrystallites possess a uniform orientation distribution, the resonance energy (or magnetic field) distribution of microcrystallites is a complex non-monotonic function that determines the specific powder pattern of the integral resonance absorption in FIRMS (or EPR) spectrum. Some turning points (extrema) of the FIRMS (or EPR) absorption lineshape and its first derivative concur with single-crystal resonant energy (or magnetic field), if the magnetic field was applied along characteristic directions, such as the *x*, *y*, or *z* axes of the *D*-tensor. The black lines in Figure 5 show calculated field dependences of such relevant turning points; b) J. A. Ibers, J. D. Swalen, *Phys. Rev.* **1962**, *127*, 1914–1917.

[38] J. Nehrkorn, J. Telser, K. Holldack, S. Stoll, A. Schnegg, *J. Phys. Chem. B* **2015**, *119*, 13816–13824.

[39] J. Bendix, M. Brorson, C. E. Schaffer, *Inorg. Chem.* **1993**, *32*, 2838–2849.

[40] J. Telser, EPR Interactions – Zero-Field Splittings, in eMagRes,Vol. 6, **2017**, pp. 207–234.

[41] The upper doublet gives $g_x(\min) = 2.28$, $g_y(\max) = 4.98$, $g_z(\mathrm{mid}) = 3.76$, which is typical of $D > 0$ ($\boldsymbol{g}_{\mathrm{eff}} = [4, 4, 2]$ for intrinsic $g = 2.00$). Thus, LFT does give the right sign.

[42] F. A. Cotton, *Chemical Applications of Group Theory*, 3 ed., Wiley, New York, **1990**, pp. Ch. 10, 304–346.

[43] C. Cohen-Tannoudji, B. Diu, F. Laloë, *Quantum Mechanics, Vol. 1*, Herman, Paris, **1977**, pp. 405–415.

[44] P.-G. Reinhard, E. Suraud, *Gross Properties and Trends, in Introduction to Cluster Dynamics*, Wiley-VCH, Weinheim, **2008**, pp. 133–178.

[45] S. Mossin, H. Weihe, A.-L. Barra, *J. Am. Chem. Soc.* **2002**, *124*, 8764–8765.

[46] a) G. N. La Mar, NMR of Paramagnetic Molecules. Principles and Applications, Academic Press, New York, **1973**, pp. 85–126; b) I. Bertini, C. Luchinat, G. Parigi, E. Ravera, NMR of Paramagnetic Molecules: Applications to Metallobiomolecules and Models, 2nd ed., Elsevier, Amsterdam, **2017**; c) F. A. Walker, NMR and EPR Spectroscopy of Paramagnetic Metalloporphyrins and Heme Proteins, in Handbook of Porphyrin Science,Vol. 6 (Eds.: K. M. Kadish, K. M. Smith, R. Guilard), World Scientific, Singapore, **2010**, pp. 1–337.

[47] A. A. Pavlov, J. Nehrkorn, S. V. Zubkevich, M. V. Fedin, K. Holldack, A. Schnegg, V. V. Novikov, *Inorg. Chem.* **2020**, *59*, 10746–10755.

[48] R. T. Azuah, L. R. Kneller, Y. Qiu, P. L. W. Tregenna-Piggott, C. M. Brown, J. R. D. Copley, R. M. Dimeo, *J. Res. Natl. Inst. Stand. Technol.* **2009**, *114*, 341–358.

[49] A. K. Hassan, L. A. Pardi, J. Krzystek, A. Sienkiewicz, P. Goy, M. Rohrer, L. C. Brunel, *J. Magn. Reson.* **2000**, *142*, 300–312.

[50] Y. Q. Cheng, L. L. Daemen, A. I. Kolesnikov, A. J. Ramirez-Cuesta, *J. Chem. Theory Comput.* **2019**, *15*, 1974–1982.

[51] a) G. Kresse, D. Joubert, *Phys. Rev. B* **1999**, *59*, 1758–1775; b) P. E. Blöchl, *Phys. Rev. B* **1994**, *50*, 17953–17979.

[52] J. P. Perdew, K. Burke, M. Ernzerhof, *Phys. Rev. Lett.* **1996**, *77*, 3865–3868.

[53] a) F. Zhou, M. Cococcioni, C. A. Marianetti, D. Morgan, G. Ceder, *Phys. Rev. B* **2004**, *70*, 235121; b) J. Chen, X. Wu, A. Selloni, *Phys. Rev. B* **2011**, *83*, 245204.

[54] J. Klimeš, D. R. Bowler, A. Michaelides, *J. Phys. Condens. Matter* **2010**, *22*, 022201.

Manuscript received: February 25, 2021
Accepted manuscript online: April 19, 2021
Version of record online: June 1, 2021

